Quadrupole collectivity in ^{42}Ca from low-energy Coulomb excitation with AGATA

K. Hadyńska-Klęk,[1,2,3,4,5,*] P. J. Napiorkowski,[1] M. Zielińska,[1,6] J. Srebrny,[1] A. Maj,[7] F. Azaiez,[8] J. J. Valiente Dobón,[4] M. Kicińska-Habior,[2] F. Nowacki,[9] H. Naïdja,[9,10,11] B. Bounthong,[9] T. R. Rodríguez,[12] G. de Angelis,[4] T. Abraham,[1] G. Anil Kumar,[7] D. Bazzacco,[13,14] M. Bellato,[13] D. Bortolato,[13] P. Bednarczyk,[7] G. Benzoni,[15] L. Berti,[4] B. Birkenbach,[16] B. Bruyneel,[16] S. Brambilla,[15] F. Camera,[15,17] J. Chavas,[6] B. Cederwall,[18] L. Charles,[9] M. Ciemała,[7] P. Cocconi,[4] P. Coleman-Smith,[19] A. Colombo,[13] A. Corsi,[15,17] F. C. L. Crespi,[15,17] D. M. Cullen,[20] A. Czermak,[7] P. Désesquelles,[21,22] D. T. Doherty,[5,6,23] B. Dulny,[7] J. Eberth,[16] E. Farnea,[13,14] B. Fornal,[7] S. Franchoo,[8] A. Gadea,[24] A. Giaz,[15,17] A. Gottardo,[4] X. Grave,[8] J. Gręboszz,[7] A. Görgen,[3] M. Gulmini,[4] T. Habermann,[10] H. Hess,[16] R. Isocrate,[13,14] J. Iwanicki,[1] G. Jaworski,[1] D. S. Judson,[25] A. Jungclaus,[26] N. Karkour,[22] M. Kmiecik,[7] D. Karpiński,[2] M. Kisieliński,[1] N. Kondratyev,[27] A. Korichi,[22] M. Komorowska,[1,2] M. Kowalczyk,[1] W. Korten,[6] M. Krzysiek,[7,28] G. Lehaut,[29] S. Leoni,[15,17] J. Ljungvall,[22] A. Lopez-Martens,[22] S. Lunardi,[13,14] G. Maron,[4] K. Mazurek,[7] R. Menegazzo,[13,14] D. Mengoni,[13] E. Merchán,[10,30] W. Męczyński,[7] C. Michelagnoli,[13,14] B. Million,[15] S. Myalski,[7] D. R. Napoli,[4] M. Niikura,[8] A. Obertelli,[6] S. F. Özmen,[1] M. Palacz,[1] L. Próchniak,[1] A. Pullia,[15,17] B. Quintana,[31] G. Rampazzo,[4] F. Recchia,[13,14] N. Redon,[29] P. Reiter,[16] D. Rosso,[4] K. Rusek,[1] E. Sahin,[4] M.-D. Salsac,[6] P.-A. Söderström,[32] I. Stefan,[8] O. Stézowski,[29] J. Styczeń,[7] Ch. Theisen,[6] N. Toniolo,[4] C. A. Ur,[13,14] R. Wadsworth,[23] B. Wasilewska,[7] A. Wiens,[16] J. L. Wood,[33] K. Wrzosek-Lipska,[1] and M. Zięblińskí[7]

[1]*Heavy Ion Laboratory, University of Warsaw, Pasteura 5A, PL 02-093 Warsaw, Poland*
[2]*Faculty of Physics, University of Warsaw, PL 00-681 Warsaw, Poland*
[3]*Department of Physics, University of Oslo, N-0316 Oslo, Norway*
[4]*INFN Laboratori Nazionali di Legnaro, Viale dell'Università, 2, I-35020 Legnaro, Italy*
[5]*Department of Physics, University of Surrey, Guildford GU2 7XH, United Kingdom*
[6]*Irfu, CEA, Université Paris-Saclay, F-91191 Gif-sur-Yvette, France*
[7]*Institute of Nuclear Physics, Polish Academy of Sciences, PL 31-342 Kraków, Poland*
[8]*Institut de Physique Nucléaire d'Orsay, F-91400 Orsay, France*
[9]*Université de Strasbourg, IPHC/CNRS, UMR7178, 23 rue du Loess, F-67037 Strasbourg, France*
[10]*GSI Helmholtzzentrum für Schwerionenforschung GmbH, D-64291 Darmstadt, Germany*
[11]*LPMS, Université Constantine 1, Route Ain-El bey, 25000 Constantine, Algeria*
[12]*Universidad Autónoma de Madrid, Departamento de Física Teórica, Madrid, Spain*
[13]*INFN Sezione di Padova, I-35131 Padova, Italy*
[14]*Dipartimento di Fisica e Astronomia dell'Università degli Studi di Padova, I-35131 Padova, Italy*
[15]*INFN Sezione di Milano, I-20133 Milano, Italy*
[16]*Institut für Kernphysik, Universität zu Köln, Zülpicher Straße 77, D-50937 Köln, Germany*
[17]*Dipartimento di Fisica dell'Università degli Studi di Milano, I-20133 Milano, Italy*
[18]*Department of Physics, Royal Institute of Technology, SE-10691 Stockholm, Sweden*
[19]*Daresbury Laboratory, Daresbury, Warrington WA4 4AD, United Kingdom*
[20]*Schuster Laboratory, School of Physics and Astronomy, The University of Manchester, Manchester, M13 9PL, United Kingdom*
[21]*Université Paris-Sud, F-91400 Orsay, France*
[22]*Centre de Sciences Nucléaires et de Sciences de la Matière (CSNSM/IN2P3/CNRS), F-91405 Orsay, France*
[23]*Department of Physics University of York, Heslington, York, YO10 5DD, United Kingdom*
[24]*Instituto de Física Corpuscular IFIC, CSIC-University of Valencia, S-46980 Paterna, Valencia, Spain*
[25]*Oliver Lodge Laboratory, The University of Liverpool, Liverpool, L69 7ZE, United Kingdom*
[26]*Instituto de Estructura de la Materia, CSIC, Madrid, E-28006 Madrid, Spain*
[27]*Flerov Laboratory of Nuclear Reactions JINR, RU-141980 Dubna, Russia*
[28]*ELI-NP, Horia Hulubei National Institute of Physics and Nuclear Engineering, 077125 Magurele, Romania*
[29]*Universite Lyon 1, CNRS, IN2P3, IPN Lyon, F-69622 Villeurbanne, France*
[30]*Technische Universität Darmstadt, D-64289 Darmstadt, Germany*
[31]*Laboratorio de Radiaciones Ionizantes, Departamento de Física Fundamental, Universidad de Salamanca, Salamanca, Spain*
[32]*Department of Physics and Astronomy, Uppsala University, SE-75120 Uppsala, Sweden*
[33]*School of Physics, Georgia Institute of Technology, Atlanta, Georgia 30332-0430, USA*

(Received 22 September 2017; published 21 February 2018)

*katarzyna.hadynska@lnl.infn.it

A Coulomb-excitation experiment to study electromagnetic properties of ^{42}Ca was performed using a 170-MeV calcium beam from the TANDEM XPU facility at INFN Laboratori Nazionali di Legnaro. γ rays from excited states in ^{42}Ca were measured with the AGATA spectrometer. The magnitudes and relative signs of ten $E2$ matrix elements coupling six low-lying states in ^{42}Ca, including the diagonal $E2$ matrix elements of 2_1^+ and 2_2^+ states, were determined using the least-squares code GOSIA. The obtained set of reduced $E2$ matrix elements was analyzed using the quadrupole sum rule method and yielded overall quadrupole deformation for $0_{1,2}^+$ and $2_{1,2}^+$ states, as well as triaxiality for $0_{1,2}^+$ states, establishing the coexistence of a weakly deformed ground-state band and highly deformed slightly triaxial sideband in ^{42}Ca. The experimental results were compared with the state-of-the-art large-scale shell-model and beyond-mean-field calculations, which reproduce well the general picture of shape coexistence in ^{42}Ca.

DOI: 10.1103/PhysRevC.97.024326

I. INTRODUCTION

Deformation of atomic nuclei is a manifestation of spontaneous symmetry breaking in a quantum many-body system, directly related to collective rotation, which was discovered in molecular physics by Jahn and Teller in 1937 [1]. Nuclear deformation can be related to the shell structure of single-particle levels in a spherical potential and, therefore, the shape evolution in atomic nuclei arises from the competition between the deformation originating from particle-vibration coupling and the pairing correlations stabilizing the nucleus in the potential energy minimum corresponding to the strongly deformed shape.

Superdeformed (SD) nuclear shapes were first observed in 1962 through the discovery of a fission isomer in ^{242}Am [2]. Ten years later, the identification of a rotational band in the second minimum of the potential energy surface in ^{240}Pu [3] proved that fission isomers indeed correspond to highly deformed nuclear shapes. This conclusion was further reinforced by lifetime measurements resulting in typical values of the transitional quadrupole moment $Q_t \approx 30\,e$ b [4] for the rotational states built on fission isomers, which corresponds to an axes ratio close to 2:1. Until now, 35 fission isomers have been identified in the actinide region.

In the late 1980s, the first superdeformed high-spin band was discovered in ^{152}Dy [5], followed by observation of very similar structures in other rare-earth nuclei, as well as in $A \sim 130$ [6,7] and $A \sim 190$ [8] mass regions. Such bands appear in the second minimum of the potential energy surface, created due to the additional energy related to the rotation of a strongly deformed shape. As the depth of the potential well decreases for lower angular momenta, the decay from the second to the first potential minimum usually occurs at spins between around $10\hbar$ and $30\hbar$. The highly fragmented nature of this decay makes it very difficult to establish a firm link between the superdeformed structures and the ground-state band, nevertheless, in a few cases this has been possible [9,10].

The phenomenon of superdeformation thus became a challenge for both experiment and nuclear structure theory, and since then about 300 SD structures have been observed in various regions of the nuclear chart [11]. Transitional quadrupole moments Q_t, measured for these structures, together with those for ground states of even-even nuclei [12], are plotted in Fig. 1. They are expected to provide a good estimate of deformation, as the SD structures behave like rigid rotors, rather weakly coupled to the yrast band in most known cases; it should be noted here that for most nonyrast structures a more sophisticated approach, such as the quadrupole sum rules method presented in Sec. IV D of the present paper, should be used. The transitional quadrupole moments presented in Fig. 1 were normalized to ZR^2 in order to remove charge dependence, as suggested, for example, in Ref. [13]. The obtained estimates of ground-state deformations, denoted by open circles, follow the $1/A^{1/3}$ dependence away from closed shells, but there are strong deviations from it in the vicinity of closed spherical shells, in particular around ^{208}Pb. The SD bands in the $A \sim 150$, $A \sim 190$, and $A \sim 230$ regions are clearly separated from normal-deformed states due to the superdeformed shell gaps, while those for $A < 150$ span a broad range of deformations and are much closer to the $1/A^{1/3}$ line.

In particular, SD bands have been recently discovered in lighter nuclei [e.g., $A \sim 60$ and lower; see Fig. 1(b)], where the number of valence particles is lower as compared to the "traditional" regions of superdeformation, and protons and neutrons may occupy the same orbitals. The value of the quadrupole deformation parameter β in the sidebands of ^{40}Ca [14,15], ^{36,38,40}Ar [16–20], and ^{44}Ti [21], as well as ^{35}Cl [22] nuclei, is between 0.4 and 0.6; see Table I. This is similar to what was previously reported for other mass regions, where superdeformation has been established. However, in contrast to heavier nuclei, strongly deformed bands in $A \sim 40$ and $A \sim 60$ isotopes extend to low spins and are linked to other, less deformed states by intense γ-ray transitions.

Considering the relatively small number of nucleons, the $A \sim 40$ mass region constitutes an excellent testing ground to study the origin of strongly deformed structures within various theoretical approaches. Superdeformation in light nuclei was discussed in the framework of large scale shell model (SM) [23,24], beyond-mean-field models (BMF) [25–27], and antisymmetrized molecular dynamics (AMD) [28–33]. In particular, the shell model was successful in describing the normal-deformed (ND) and SD structures in ^{40}Ca, with the calculations yielding a spherical ground-state band, a ND band ($\beta = 0.3$) built on the 0_2^+ state dominated by the $4p-4h$ excitation into the pf shell, and a SD band ($\beta = 0.6$) built on the 0_3^+ state with an $8p-8h$ configuration [24].

Experimental deformation parameters of known superdeformed bands in the $A \sim 40$ mass region, and their dominant configurations resulting from shell-model calculations are presented in Table I.

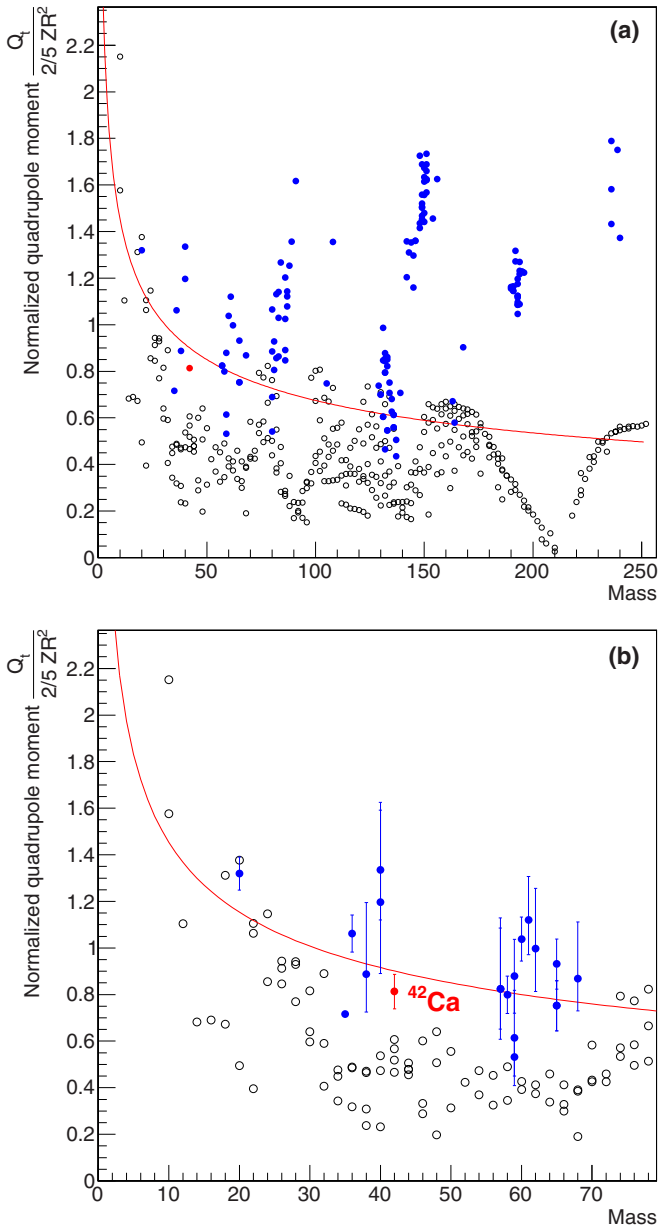

FIG. 1. Experimental values of transitional quadrupole moments Q_t, normalized to ZR^2 to remove the Z dependence, for ground-state bands (open circles [12]), and superdeformed bands (filled circles [11]). The values for superdeformed bands in the $A \sim 40$ mass region are taken from references listed in Table I. The solid line represents the $1/A^{1/3}$ dependence and is scaled to experimental values for midshell nuclei. Uncertainties of the values for ground-state bands are not plotted for clarity, as well as those for superdeformed bands in panel (a). Panel (a) presents all available data, while panel (b) is zoomed in on the $A < 70$ mass region. Our recent result for the 0_2^+ state in ^{42}Ca [34] is presented in red.

In a recent paper [34] we reported on the results of a dedicated Coulomb-excitation experiment to study the electromagnetic structure of ^{42}Ca, which provided firm evidence for the superdeformed character of the sideband in this nucleus, as well as its slight triaxiality. This result was consistent with the earlier observations suggesting a highly deformed character for this structure. First, its moment of inertia, which is proportional to the quadrupole deformation parameter β_2 [35], is large and similar to those in the SD bands in both ^{36}Ar and ^{40}Ca. Furthermore, this band was preferentially fed by the low-energy component of the highly split giant dipole resonance decay of ^{46}Ti [36]. On the other hand, the bandhead of the sideband in ^{42}Ca lies at excitation energy of 1837 keV, considerably lower than its counterparts in the neighboring Ca and Ar isotopes, and so it was possible to populate this structure with Coulomb excitation in order to obtain a complete set of electromagnetic matrix elements between the observed states. In the present paper we provide a more in-depth description of the experiment, the data analysis procedure, and the theoretical calculations. It is organized as follows: the experiments are presented in Sec. II, while the details of of the Coulomb-excitation data analysis and the final results are described in Sec. III. In Sec. IV the theoretical approaches and interpretation are presented. In Sec. IV D the quadrupole sum rules method is introduced and the obtained quadrupole shape parameters of the low-lying states in ^{42}Ca are discussed.

TABLE I. Experimentally determined β_2 deformation parameters in known superdeformed bands in the $A \sim 40$ region, and their dominant shell-model configurations.

Isotope	Experimental β_2 value	Configuration
^{40}Ca [14,15]	$0.59^{+0.11}_{-0.07}$	$8p-8h$
^{36}Ar [16,17]	0.46 ± 0.03	$4p-8h$
^{38}Ar [18,19]	$0.42^{+0.11}_{-0.08}$	$4p-6h$
^{40}Ar [20]	$0.48^{+0.16}_{-0.10} \pm 0.05$	$4p-4h$
^{44}Ti [21]	not known	$8p-4h$
^{35}Cl [22]	0.37	$3p-3h$
^{42}Ca [34]	0.43(4) (0_2^+)	$6p-4h$
	0.45(4) (2_2^+)	$6p-4h$

II. EXPERIMENTAL DETAILS

A Coulomb-excitation experiment to study the electromagnetic structure and deformation of ^{42}Ca was performed at the INFN Laboratori Nazionali di Legnaro, Italy [37,38].

A continuous ^{42}Ca beam of 170 MeV energy and 1 pnA intensity was delivered by the TANDEM XPU accelerator and bombarded a 1-mg/cm^2-thick ^{208}Pb target, enriched to 99%, and a natural ^{197}Au target of the same thickness. In order to maximize population of the higher-lying states in ^{42}Ca, the beam energy was chosen to be as close as possible to the maximum energy allowed by the Cline's "safe energy" criterion [39] and corresponded to 98.7% of the "safe energy" for ^{42}Ca + ^{208}Pb and 100.5% for ^{42}Ca + ^{197}Au, for the maximum scattering angle covered by the particle detection system (142°).

The γ rays from Coulomb-excited nuclei were measured with the three triple clusters of AGATA [40] placed at 14.3 cm from the target for the runs with ^{208}Pb target and 19.5 cm for

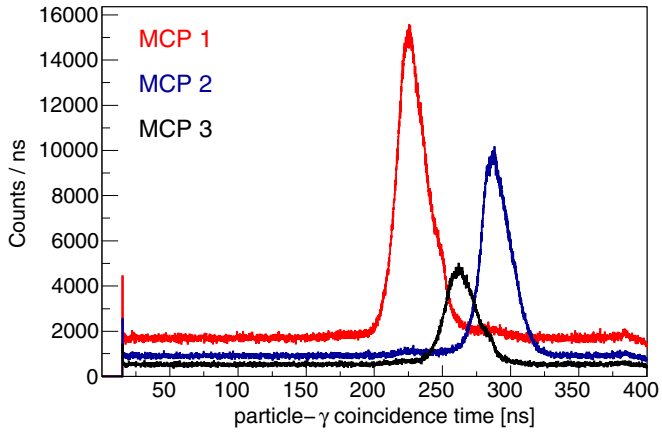

FIG. 2. Particle-γ coincidence time spectra for the three MCP detectors of the DANTE array.

^{197}Au. The center of AGATA pointed at 63° with respect to the beam direction.

The data were collected for 5 days requiring coincidence between γ rays and back-scattered ^{42}Ca ions, detected in the DANTE array [41,42]. This setup consisted of three position-sensitive microchannel plate (MCP) detectors, of dimensions 40 mm × 60 mm and 13 mm thick, covering θ_{LAB} angles from 100° to 144° with respect to the beam direction. The useful detection range, without taking into account the inactive area at the detector borders, was 105 to 142°.

Data acquisition of the AGATA array was fully digital, while signals from the MCP detectors were processed by analog electronics. The readout of DANTE was synchronized and merged with the AGATA acquisition system using the AGAVA interface [40].

The energy and efficiency calibration of the AGATA array in the range up to 2.6 MeV was performed under conditions identical to those in the Coulomb-excitation experiment, using ^{152}Eu and ^{226}Ra γ-ray sources placed at the target position. The position calibration of the MCP detectors was performed using an ^{241}Am source and markers placed on the surface of the detectors.

Events were collected with a condition that at least one γ ray was registered in AGATA together with exactly one ^{42}Ca ion detected in one of the MCP detectors within a 400-ns coincidence window. Gates on the particle-γ prompt coincidence peak were set individually for each MCP detector (see Fig. 2).

The kinematic information from the position-sensitive detectors of the DANTE array was used to Doppler correct the energies of γ rays depopulating Coulomb-excited states in ^{42}Ca. The γ-ray spectrum obtained with the ^{208}Pb target, Doppler-corrected for the ^{42}Ca velocity, is shown in Fig. 4. It was collected in coincidence with back-scattered particles registered in one of the MCP detectors.

In the experiment the following transitions in ^{42}Ca were observed: $2_1^+ \rightarrow 0_1^+$ (1525 keV), $4_1^+ \rightarrow 2_1^+$ (1227 keV), $2_2^+ \rightarrow 2_1^+$ (899 keV), $2_2^+ \rightarrow 0_1^+$ (2424 keV), $4_2^+ \rightarrow 2_1^+$ (1729 keV), and $0_2^+ \rightarrow 2_1^+$ (312 keV). These transitions are marked in red in Fig. 3. Their intensities are presented in Table II. Additionally,

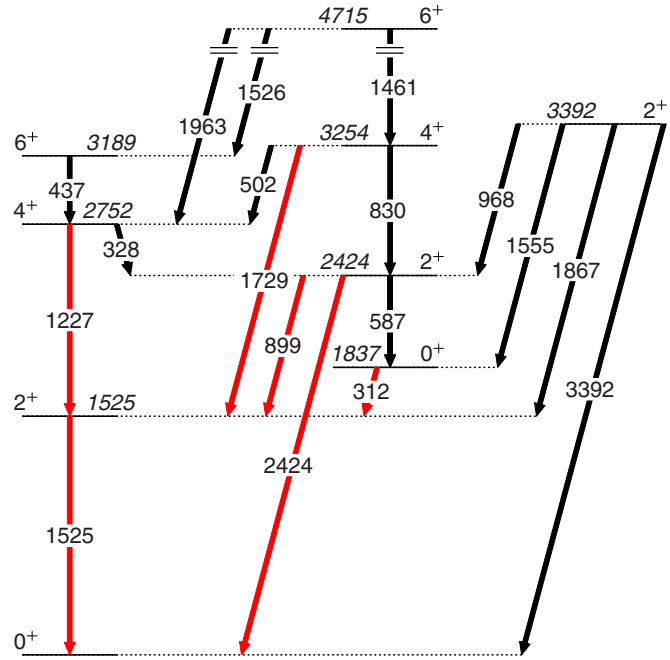

FIG. 3. Low-lying excited states in ^{42}Ca, considered in the present analysis. Transitions observed in the current experiment are marked in red. Level and transition energies are given in keV. Reproduced from Ref. [34].

the excitation of the 6_1^+ state at 3189 keV was observed, but since the lifetime of this state, equal to 7.8(2) ns, is longer than the average time of flight between the target and the particle detector, the weak $6_1^+ \rightarrow 4_1^+$ transition has been completely smeared out when applying Doppler correction.

A Doppler-broadened and shifted 511-keV γ-ray line, and transitions from Coulomb excitation of target impurities, ^{204}Pb (899 keV), ^{206}Pb (803 keV), ^{207}Pb (570 keV), are also present in the experimental spectrum. In particular, the

TABLE II. Numbers of counts in the observed γ-ray transitions in ^{42}Ca, and their relative intensities (corrected for efficiency) normalized to that of the $2_1^+ \rightarrow 0_1^+$ transition.

I_i^π	I_f^π	Energy (keV)	Number of counts	Intensity
		^{208}Pb target		
2_1^+	0_1^+	1525	$1.08(8) \times 10^6$	100(8)
4_1^+	2_1^+	1227	$1.07(8) \times 10^4$	0.93(7)
0_2^+	2_1^+	312	$1.14(5) \times 10^5$	6.9(3)
2_2^+	0_1^+	2424	$2.7(7) \times 10^3$	0.28(8)
4_2^+	2_1^+	1729	$2.9(8) \times 10^3$	0.28(8)
		^{197}Au target		
2_1^+	0_1^+	1525	$9.2(8) \times 10^4$	100(10)
4_1^+	2_1^+	1227	$1.30(12) \times 10^3$	1.29 (13)
0_2^+	2_1^+	312	$9.7(7) \times 10^3$	6.9(5)
2_2^+	0_1^+	2424	300(140)	0.39(19)
2_2^+	2_1^+	899	$1.12(10) \times 10^3$	0.99(10)
4_2^+	2_1^+	1729	400(110)	0.45(13)

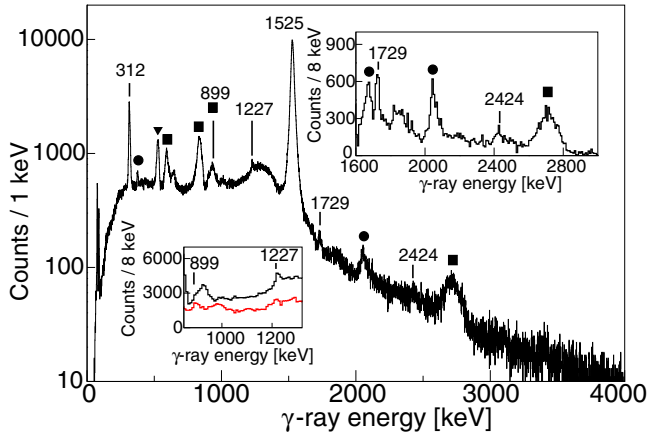

FIG. 4. The γ-ray spectrum observed in the ^{42}Ca + ^{208}Pb Coulomb-excitation experiment in coincidence with back-scattered particles registered in one of MCP detectors, Doppler-corrected for the projectile. The lines not originating from ^{42}Ca (see text for details) are marked as follows: ■, lead isotopes; ▼, 511 keV; ●, ^{43}Ca. Insets show portions of the spectrum zoomed on the 1600–3000-keV and 850–1300-keV energy ranges, the latter presenting also the spectrum collected with the ^{197}Au target (in red, multiplied by a factor of 3 for presentation purpose).

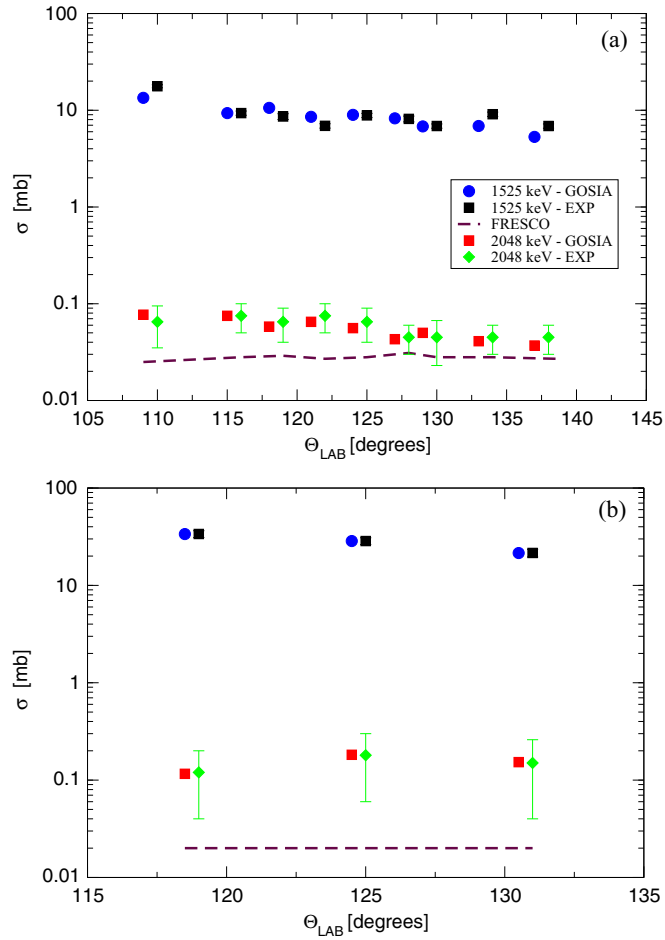

FIG. 5. Experimentally measured cross sections compared to the results of calculations with the GOSIA and DWBA codes (FRESCO). Panel (a) ^{42}Ca on ^{208}Pb; (b) ^{42}Ca on ^{197}Au. The points are slightly offset on the x axis for clarity.

Doppler-broadened transition in ^{204}Pb obscured the $2_2^+ \rightarrow 2_1^+$ line in ^{42}Ca, and, consequently, the intensity of this transition in data collected using the Pb target could not be included in the Coulomb-excitation analysis. The ^{197}Au target was meant to be used mostly to set up proper particle-γ coincidences, and as a consequence much lower statistics were collected using this target. In this case, however, the 899-keV peak was not contaminated by any transitions resulting from target excitation (see inset of Fig. 4), hence its intensity could be determined with a good precision.

A. Sub-barrier transfer reaction

In addition to the transitions resulting from Coulomb excitation of ^{42}Ca and lead isotopes, weaker lines at 376, 1674, and 2048 keV were observed. These could originate from Coulomb excitation of unknown states in ^{42}Ca, or from a different reaction. Both these hypotheses appeared unlikely, as the low-spin part of the level scheme of ^{42}Ca seemed to be well known, and the experiment was performed at a beam energy which did not exceed the strict Cline's "safe energy" criterion [39] for ^{42}Ca + ^{208}Pb, thus no processes other than safe Coulomb excitation were likely to occur. However, a 2048-keV transition is present in the decay scheme of ^{43}Ca, related to the deexcitation of the $p_{3/2}$ single particle state. Two scenarios were therefore tested: that the 376- and 2048-keV γ-ray lines resulted from the decay of a Coulomb-excited 2^+ state at 2048 keV excitation energy, previously unknown, or that they originated from the ^{208}Pb(^{42}Ca,^{43}Ca)^{207}Pb transfer reaction at about 70% of the Coulomb barrier. Consequently, the angular distribution of the most intense of these γ-ray transitions, 2048 keV, was analyzed in order to compare with what would be expected for the sub-barrier neutron transfer reaction ^{208}Pb(^{42}Ca,^{43}Ca)^{207}Pb, and for the Coulomb-excitation process. To this end, the range of scattering angles covered by each of the MCP particle detectors was divided into three bins:

(i) (105°–114°), (114°–123°), (123°–132°) for MCP 1,
(ii) (111°–120°), (120°–129°), (129°–138°) for MCP 2,
(iii) (118–126°), (126°–134°), (134°–142°) for MCP 3.

Since the $B(E2; 2_1^+ \rightarrow 0_1^+)$ value in ^{42}Ca, as well as the spectroscopic quadrupole moment of the 2_1^+ state are well known, it was possible to use this line for normalization of the measured cross sections: the intensity of the $2_1^+ \rightarrow 0_1^+$ transition, measured for each bin of scattering angle, was compared with the excitation cross section, calculated for the 2_1^+ state using the GOSIA code. The resulting normalization was applied to the measured intensity of the 2048-keV transition in order to obtain the absolute experimental cross section as a function of scattering angle. Those were compared with the results of two calculations: Coulomb-excitation cross section to populate an unknown 2^+ state at 2048 keV, estimated using the GOSIA code, and with one-neutron transfer reaction calculations to populate the $p_{3/2}$ state in ^{43}Ca, performed by means of distorted-wave Born approximation (DWBA)

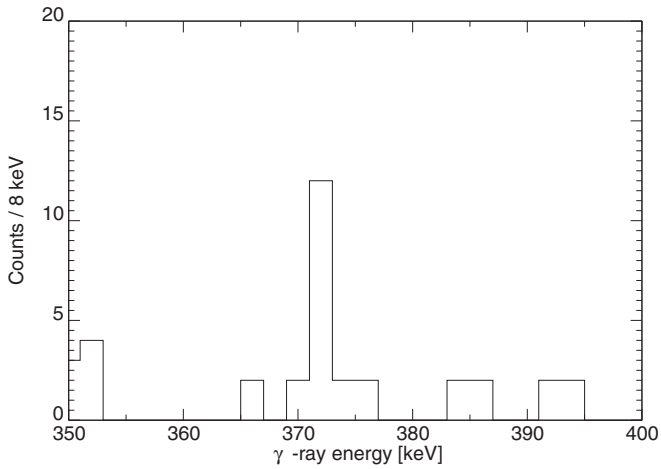

FIG. 6. The γ-γ spectrum gated on the 570-keV γ-ray transition in ^{207}Pb. The 373-keV γ-ray line originating from ^{43}Ca is shown.

method using the FRESCO code [43]. The results are plotted in Fig. 5(a). In the DWBA predictions, the optical model potentials in the entrance and exit channels were taken from the global parametrization of Broglia and Winther [44] and the spectroscopic factors for the target nucleus and the ejectile were set to unity.

The observed ratio of the 376- and 2048-keV transition intensities in the present experimental spectra was around 30%, similar to the ratio of the 373- and 2046-keV γ-ray transitions in ^{43}Ca observed in the (d,p) reaction, which equals 32% [45]. The Q value for the ^{208}Pb(^{42}Ca,^{43}Ca)^{207}Pb reaction is positive and equal to 565 keV, supporting the transfer scenario. On the other hand, the angular distribution of the 2048-keV γ line fits better to the Coulomb-excitation predictions than to the transfer calculations, as demonstrated in Fig. 5.

Additionally, γ-γ coincidences were analyzed. The γ-γ matrix was constructed with the γ rays Doppler corrected for the projectile velocity on one axis, and the γ rays Doppler corrected for the recoil velocity on the other. A coincidence gate set on the 570-keV γ-ray transition deexciting the first excited state in ^{207}Pb showed the 373-keV γ-ray line in ^{43}Ca, as presented in Fig. 6, providing a strong evidence for the one-neutron transfer reaction.

The data collected with the ^{197}Au target were used for a cross-check. Although the level of statistics in this measurement was low, it was sufficient to observe the 2048-keV γ-ray transition. Hence, the possibility of one-neutron transfer reaction ^{197}Au(^{42}Ca,^{43}Ca)^{196}Au was taken into consideration, although the Q value is negative (-140 keV).

As in the case of data collected with the Pb target, the angular distribution of γ rays related to scattered calcium projectiles was analyzed. Due to the lower statistics, the data were subdivided into only three ranges of scattering angles in the laboratory frame:

(i) 105°–132° for MCP 1,
(ii) 111°–138° for MCP 2,
(iii) 118°–142° for MCP 3.

Figure 5(b) presents again the comparison of experimentally determined cross sections related to the 2048-keV transition with the estimates obtained using the GOSIA code and those for the $1n$ transfer cross section calculated within the DWBA approach. As for the ^{208}Pb target, in the DWBA calculations the optical model potentials were taken from Ref. [44] and the spectroscopic factors set to unity. In this case, the experimental 2048-keV γ-ray yields and the cross section calculated using the FRESCO code differ by one order of magnitude. The present DWBA calculations, though, can only be understood as rough estimates, since the relevant optical potentials at the experimental energies and the spectroscopic factors for states in ^{43}Ca and the target nuclei are not precisely known. The angular distributions are in this case more meaningful than the absolute cross sections, and unfortunately, due to the much lower statistics, no conclusion can be drawn from those measured for the ^{197}Au target.

The arguments supporting the sub-barier transfer hypothesis needed additional validation. A dedicated measurement to verify the known level scheme of ^{42}Ca has been performed and its detailed description is presented in the following section.

B. Verification of the low-spin structure of ^{42}Ca in a fusion-evaporation experiment

As the measured angular distributions of the 2048-keV transition were better described by Coulomb excitation than by transfer calculations (see Fig. 5), and a presence of an additional state at low excitation energy would influence the results of the Coulomb-excitation analysis, it was decided that it would be prudent to perform an experimental verification of the low-spin level scheme of ^{42}Ca. A dedicated fusion-evaporation experiment was performed at the Heavy Ion Laboratory, University of Warsaw [38], using the EAGLE spectrometer [46] consisting of 15 high-purity germanium (HPGe) detectors equipped with anti-Compton BGO shields. Germanium detectors were placed at the following laboratory angles with respect to the beam direction: 25° (1 Ge detector), 38° (2), 63° (2), 90° (2), 117° (2), 142° (2), and 155° (1).

A ^{32}S beam of 80 MeV energy bombarded a 100-mg/cm^2-thick ^{12}C target. Significant production of ^{42}Ca was observed in the $2p$ reaction channel, although it led mostly to the population of states in the yrast band. The states in the sideband in ^{42}Ca, including the 2424-keV level, were populated in the β decay of ^{42}Sc, produced in the pn evaporation channel. In its ground state, ^{42}Sc has a half-life of 681.3 ms and $J^\pi = 0^+$, whereas its isomeric state ^{42}Sc^m has a spin $J^\pi = 7^+$, and a longer lifetime of $T_{1/2} = 61.8$ s. ^{42}Sc^m β decays in 100% to the 6_1^+ level in ^{42}Ca, which promptly emits three γ rays in a cascade: 437 keV ($6_1^+ \rightarrow 4_1^+$), 1227 keV ($4_1^+ \rightarrow 2_1^+$), and 1524 keV ($2_1^+ \rightarrow 0_1^+$). However, the 4_1^+ state at 2752 keV decays also to the 2_2^+ state at 2424 keV, with the emission of a 328-keV γ ray. In the experiment, both the 2424- and 899-keV transitions deexciting the 2_2^+ state were observed (see Fig. 7), which verified this part of the level scheme of ^{42}Ca and also allowed determination of the $2_2^+ \rightarrow 0_1^+$ / $2_2^+ \rightarrow 2_1^+$ branching ratio. The obtained value, 0.35(7), which is in agreement with the previous findings [47,48], was used to constrain the Coulomb-excitation data analysis described in the following section.

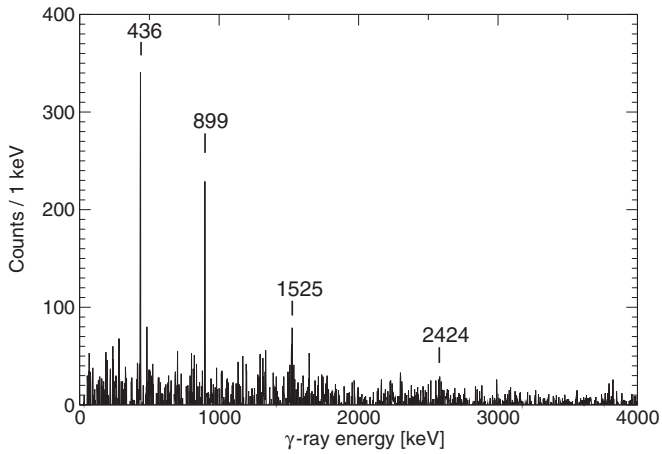

FIG. 7. The γ-ray spectrum collected in the $^{12}C + ^{32}S$ experiment, gated on the 328-keV transition deexciting 4_1^+ state in ^{42}Ca.

None of the 373-, 1674-, and 2046-keV γ-ray transitions present in the Coulomb-excitation spectra have been observed in the fusion-evaporation experiment, which further confirms that they originate from one-neutron transfer.

It should be noted that the Cline's criterion [39], fulfilled in the present study for ^{42}Ca + ^{208}Pb, is supposed to ensure that less than 0.5% of the total reaction cross section arises from processes other that safe Coulomb excitation. The ratio of the experimentally measured cross section to populate the $p_{3/2}$ state in ^{43}Ca via the ^{208}Pb(^{42}Ca,^{43}Ca)^{207}Pb transfer reaction to that to populate the 2_1^+ state in Coulomb excitation is equal to 0.9%. We do not expect that this effect may change the conclusions of the present paper, in particular the $E2$ matrix elements extracted from the measured transition intensities, as the role of other reaction channels remains negligible as compared to safe Coulomb excitation. It means, however, that for certain combinations of beams and targets the Cline's criterion may not work as well as one might imagine.

III. COULOMB-EXCITATION DATA ANALYSIS

A set of reduced electromagnetic matrix elements between the low-lying states in ^{42}Ca was extracted from the Coulomb-excitation data using the GOSIA code [49,50]. The level scheme of ^{42}Ca which was considered in the current analysis is presented in Fig. 3. It is known from the following reactions:

(i) Coulomb excitation [51];
(ii) β decay of ^{42}K [52–54] and ^{42}Sc [55–59];
(iii) reactions induced by heavy ions: ^{28}Si(^{19}F, $p\alpha$)^{42}Ca [60], ^{27}Al(^{18}O, $p2n$)^{42}Ca [61], ^{27}Al(^{19}F,$\alpha\gamma$)^{42}Ca [62], ^{28}Si(^{16}O,$2p\gamma$)^{42}Ca [63–65], ^{40}Ca(^{12}C,^{10}C)^{42}Ca [66];
(iv) reactions induced by light ions: (d,t), (^{3}He,d) and (α,p) [48,67–72], $(\alpha$,p) [73] $(\alpha,2p)$ [74], (t,p) [75];
(v) inelastic scattering: (γ,γ') [76], $(p,p'\gamma)$ [47,77].

From the experiments listed above, branching ratios [47,52,57,78] and $E2/M1$ mixing ratios [66,79] were determined (see Table IV). For the $2_2^+ \to 0_1^+/2_2^+ \to 2_1^+$ branching ratio, the new value determined in the experiment described in Sec. II B was used. Those, together with the known lifetimes of yrast and nonyrast states, summarized in Table III, were used in the GOSIA analysis as additional data points, entering the multidimensional χ^2 fit in the same way as the γ-ray intensities measured in the current Coulomb-excitation experiment. This increased the sensitivity to higher-order effects such as spectroscopic quadrupole moments and relative signs of matrix elements, as well as to the influence of nonobserved transitions on the measured excitation cross sections, in particular that of the $2_2^+ \to 0_2^+$ transition.

TABLE III. Lifetimes of the excited states in ^{42}Ca used as additional data points in the present Coulomb-excitation data analysis.

I_i^π	τ (ps)	Measurement
2_1^+	1.19(4)	[51]
4_1^+	4.45(40)	[61,65]
6_1^+	7790(140)	[59,72,74]
0_2^+	558(8)	[77]
2_2^+	0.18(4)	[47,72]
4_2^+	0.18(3)	[80]
6_2^+	0.120(46)	[71]
2_3^+	0.17(3)	[80]

For the lifetime of the 2_1^+ state at 1525 keV, the value extracted from $B(E2;0_1^+ \to 2_1^+)$ measured in a one-step Coulomb-excitation experiment with a ^{32}S beam [51] was used in the current data analysis. In this measurement, the state of interest was populated from below, and possible influence of multistep excitation of higher-lying states was well controlled and taken into account in the data analysis. This lifetime was also measured with the Doppler-shift attenuation method (DSAM) [72], yielding a value of 0.75(30) ps, but subject to a much larger uncertainty than the Coulomb-excitation result [51]. As the sources of possible systematic error seemed to be much better controlled in the case of the Coulomb-excitation experiment [51], the value resulting from the DSAM measurement has not been considered in the current data analysis.

The lifetime of the 4_1^+ state at 2754 keV was measured in several recoil-distance method (RDM) experiments following fusion-evaporation reactions, yielding results of 3.8(4) ps [65], 5.1(4) ps [60], 2.3(10) ps [70], and 5.1(4) ps [61]. However, Ref. [60] reported a problem with the feeding of the 4_1^+ state, and consequently the resulting value was not taken into account. Two more existing values were rejected: 3.4(-17, $+110$) ps and 2.3(10) ps obtained using DSAM in Refs. [47] and [70], respectively, because of very large uncertainties, and 11.5(25) ps from a RDM measurement following (α, p) transfer [69], as the authors reported high background due to feeding from the long-lived 6^+ state. In the end, the weighted average value of the results obtained in Refs. [65] and [61] was used in the present Coulomb-excitation analysis.

The 6_1^+ state at 3189 keV has a much longer lifetime than the other states in ^{42}Ca. In the present data analysis, it was decided to use the weighted average value of the results obtained using the differential perturbed angular correlation

method [7.65(23) ns [73]] and positron-γ coincidences [7.96 (22) ns [59], 7.76(26) ns [74], and 7.8(10) ns [72]].

The lifetime of the 0_2^+ state at 1837 keV was determined in a $p-\gamma$ coincidence measurement performed using a direct electronic timing technique following a ^{42}Ca$(p,p'\gamma)$ reaction [77] to be equal to 558(8) ps. This value had a much smaller uncertainty and deviated more than 2σ from that obtained in a delayed β-γ-γ coincidence experiment [480(30) ps [53]], hence we concluded that the former method was more appropriate in this case and thus the result of Ref. [77] was used in the current analysis.

For the 2_2^+ state at 2424 keV, a weighted average of the lifetimes determined in two DSAM experiments [47,72] was used, as they were both performed under similar conditions and the obtained precision was similar [0.30(+3,−4) and 0.16(4) ps, respectively].

The lifetime of the 4_2^+ state at 3254 keV was measured in three DSAM experiments [47,72,80] under similar experimental conditions, yielding 0.30(+15,−10) ps [47], 0.15(4) ps [72], and 0.18(3) ps [80]. The obtained values agree within error bars, although that reported in Ref. [47] has a considerably lower precision than two later measurements. In the Coulex analysis, the most recent and at the same time most precise value, 0.18(3) ps, [80] was used.

The lifetime of the 6_2^+ state at 4715 keV was determined in a DSAM measurement [71] to be equal to 120(46) fs. The same technique was used to measure the lifetime of the 2_3^+ state at 3392 keV equal to 0.17(3) ps [80].

The spectroscopic quadrupole moment of the 2_1^+ state in ^{42}Ca, equal to $-19(8)$ e fm^2, was determined using the reorientation effect in Coulomb excitation [51]. The $2_1^+ \rightarrow 0_1^+$ γ-ray intensities, measured for several scattering angles, were analyzed using the coupled-channels code of de Boer and Winther [81]. In the calculations, the ground state and states at 1.524 (2_1^+), 1.836 (0_2^+), 2.422 (2_2^+), and 2.75 MeV (4_1^+) were included, with $E2$ transitional matrix elements taken from Refs. [47,80].

The 0_2^+ state decays almost exclusively to the 2_1^+ state with the emission of a 312-keV γ ray, however, an electric monopole transition, $0_2^+ \rightarrow 0_1^+$, is also known [77,82–84]. The ratio of $0_2^+ \rightarrow 0_1^+/0_2^+ \rightarrow 2_1^+$ electron intensities was determined to be equal to 1.03(10) in a $(p,p'\gamma)$ study [82]. This is equivalent to the $I(E0;0_2^+ \rightarrow 0_1^+)/I(E2;0_2^+ \rightarrow 2_1^+)$ branching of 0.35%. It was decided to include this decay path in the Coulomb-excitation data analysis for completeness, even though the effect is small. Since this information cannot be directly introduced into the GOSIA input files, an indirect method described in Ref. [85] was used: a virtual level of spin and parity 1^+, at arbitrarily chosen 1200-keV excitation energy, has been declared in addition to the known level scheme of ^{42}Ca, and connected to the 0_2^+ state by a $M1$ transition. The $\langle 1^+\|M1\|0_2^+\rangle$ was fitted so that the relative intensity of the $0_2^+ \rightarrow 1^+$ transition was equal to the relative intensity of $E0$ electrons measured in Ref. [82]. The introduction of such a level does not affect the observed excitation pattern, as low-energy Coulomb excitation proceeds predominantly via $E2$ transitions; it, however, accounts for the alternative decay path of the 0_2^+ state.

TABLE IV. Relative intensities of the γ-ray transitions and mixing ratios δ for mixed $E2/M1$ transitions in ^{42}Ca used as additional data points in the present Coulomb-excitation data analysis.

I_i^π	I_j^π	E_γ (keV)	Relative intensity
2_2^+	2_1^+	899	1
2_2^+	0_1^+	2424	0.35(7)
2_2^+	0_2^+	587	0.007(3)
4_1^+	2_1^+	1227	1
4_1^+	2_2^+	328	0.010(4)
4_2^+	2_1^+	1729	1
4_2^+	2_2^+	830	0.18(9)
4_2^+	4_1^+	502	0.64(9)
6_2^+	4_1^+	1963	1
6_2^+	4_2^+	1461	0.94(6)
6_2^+	6_1^+	1526	0.15(4)
2_3^+	2_1^+	1867	1
2_3^+	0_1^+	3392	0.90(6)
2_3^+	0_2^+	1555	0.12(4)
2_3^+	2_2^+	968	0.05(4)
I_i^π	I_j^π	E_γ (keV)	$\delta(E2/M1)$
2_2^+	2_1^+	899	−0.18(2)
2_3^+	2_1^+	1867	1.7(4)

In the GOSIA χ^2 fitting procedure, Coulomb-excitation amplitudes for all declared states are calculated for a given set of matrix elements and the scattering kinematics, defined by the particle and γ-ray detection geometries. The subsequent calculation of γ-ray decay takes into account effects such as internal conversion, the finite size and relative efficiency of Ge detectors, and the attenuation caused by the deorientation effect during recoil into vacuum. In order to compare the experimentally observed and the calculated γ-ray intensities, the latter are integrated over the range of scattering angles covered by the particle detectors, as well over the range of incident energies due to the beam slowing down in the target material.

The χ^2 fit of the observed γ-ray yields (Table II) and other spectroscopic data (Tables III and IV) was performed with 26 $E2$ and 4 $M1$ matrix elements.

In particular, although no transitions deexciting the 2_3^+ state were observed in the present experiment, its influence on the population of other states was taken into account by introducing into the calculations six matrix elements coupling it to the observed states. These were calculated from the known spectroscopic data, such as the lifetime of the 2_3^+ state, branching ratios for all possible paths of its decay, and the $2_3^+ \rightarrow 2_1^+$ mixing ratio (see Table IV), and remained fixed in the GOSIA minimization routine. The $2_3^+ \rightarrow 2_2^+$ transition, for which no $E2/M1$ multipole mixing ratio was known, was assumed to be of pure $E2$ character.

The relative signs of matrix elements may have a significant influence on Coulomb-excitation cross sections, as illustrated for example by Fig. 3 of Ref. [86]. The signs and magnitudes of the experimental matrix elements reported in the present work

TABLE V. Reduced transitional and diagonal $E2$ matrix elements between the low-lying states in ^{42}Ca, and corresponding $B(E2)$ values and spectroscopic quadrupole moments determined in the course of the present analysis. Present experimental results are compared with previously measured values, large-scale shell-model (SM) and beyond-mean-field (BMF) calculations, as well as the $\alpha + {}^{38}$Ar orthogonality condition model (OCM) predictions [87].

$I_i^+ \rightarrow I_f^+$	$\langle I_i \Vert E2 \Vert I_f \rangle$ (e fm^2)			$B(E2\downarrow; I_i^+ \rightarrow I_f^+)$ (W.u.)[a]				
	Present	SM	BMF	Present	Previous	SM	BMF	OCM [87]
$2_1^+ \rightarrow 0_1^+$	$20.5^{+0.6}_{-0.6}$	11.5	9.14	$9.7^{+0.6}_{-0.6}$	9.3 ± 1 [51] 11 ± 2 [79] 9 ± 3 [80] 8.5 ± 1.9 [47]	3.05	1.9	5.6
$4_1^+ \rightarrow 2_1^+$	$24.3^{+1.2}_{-1.2}$	11.3	12.2	$7.6^{+0.7}_{-0.7}$	6.8 ± 0.6 [61] 8.7 ± 0.9 [65] 10^{+10}_{-8} [47] 18 ± 7 [70] 11 ± 3 [80] 50 ± 15 [79]	1.6	1.85	7.3
$0_2^+ \rightarrow 2_1^+$	$22.2^{+1.1}_{-1.1}$	11.9	6.1	57^{+6}_{-6}	64 ± 4 [80] 100 ± 6 [79] 55 ± 1 [77] 64 ± 4 [47]	16.3	4.3	3.5
$2_2^+ \rightarrow 0_1^+$	$-6.4^{+0.3}_{-0.3}$	9.4	4.4	$1.0^{+0.1}_{-0.1}$	2.2 ± 0.6 [79] 1.5 ± 0.5 [80] 1.2 ± 0.3 [47]	2.04	0.5	0.35
$2_2^+ \rightarrow 2_1^+$	$-23.7^{+2.3}_{-2.7}$	-13.6	-7.7	$12.9^{+2.5}_{-2.5}$	17 ± 11 [79] 19^{+22}_{-14} [80] 14^{+35}_{-9} [47]	4.3	1.4	0.83
$4_2^+ \rightarrow 2_1^+$	42^{+3}_{-4}	21.9	10.1	23^{+3}_{-4}	30 ± 11 [79] 16 ± 5 [80] 12^{+7}_{-4} [47]	6.3	1.3	0.11
$2_2^+ \rightarrow 0_2^+$	26^{+5}_{-3}	32	42	15^{+6}_{-4}	<61 [80] <46 [47]	24	40.7	37
$4_2^+ \rightarrow 2_2^+$	46^{+3}_{-6}	52	70	27^{+4}_{-6}	60 ± 30 [80] 60 ± 20 [79] 40^{+40}_{-30} [47]	35	63	35.7
	$\langle I_i \Vert E2 \Vert I_i \rangle$ (e fm^2)					Q_{sp} (e fm^2)		
2_1^+	-16^{+9}_{-3}	-4.3	0.1	-12^{+7}_{-2}	-19 ± 8 [51]	-3	0.5	-14.3
2_2^+	-55^{+15}_{-15}	-31	-42	-42^{+12}_{-12}		-23	-32	

[a]For ^{42}Ca, 1 W.u. $= 8.67\ e^2$ fm^4.

were carefully verified by performing the χ^2 minimization procedure starting from different initial sets of matrix elements, and comparing the quality of resulting fits. For example, imposing a positive sign for the $\langle 0_1^+ \Vert E2 \Vert 2_2^+ \rangle$ matrix element resulted in an immediate 11-fold increase of the obtained χ^2 value.

The following sign convention has been imposed: signs of all in-band transitional $E2$ matrix elements, both in the ground-state band and in the sideband, were assumed to be positive, as well as that of $\langle 0_2^+ \Vert E2 \Vert 2_1^+ \rangle$. Signs of all other $E2$ matrix elements have been determined relative to those.

The experiment had no sensitivity to the signs of matrix elements involving the 2_3^+ state; they were assumed to be positive, consistent with the large-scale shell-model predictions.

The resulting set of reduced matrix elements in ^{42}Ca together with their relative signs and the corresponding $B(E2)$ values are presented in Table V. In addition, in Table VI we present a list of $E2$ and $M1$ matrix elements that were determined from other spectroscopic data, and their values corresponding to the final solution of the GOSIA minimization procedure.

The statistical errors of the matrix elements were calculated when the convergence of the χ^2 minimization was achieved. This was performed in two steps. First, the χ^2 surface is sampled in the vicinity of the minimum, using different values of the matrix element in question, with all other matrix elements remaining fixed, in order to find the "diagonal" uncertainty. Second, possible correlations between all matrix elements are taken into account, in order to obtain the total statistical uncertainty. Note that we do not present uncertainties of matrix elements in Table VI; this is to avoid creating false impression that these specific matrix elements have been independently determined from the present Coulomb-excitation data. Their uncertainties, used for example to calculate the uncertainties of shape parameters in Sec. IV D, are calculated from the

TABLE VI. Reduced transitional $E2$ and $M1$ matrix elements between the low-lying states in ^{42}Ca, included in the present analysis, and corresponding $B(E2)$ and $B(M1)$ values. These matrix elements were not determined from the present data set, but they influence the extraction of matrix elements listed in Table V. The values corresponding to the final solution of the GOSIA fit are compared with the results of previous measurements, large-scale shell-model (SM) and beyond-mean-field (BMF) calculations, as well as the $\alpha + {}^{38}$Ar orthogonality condition model (OCM) predictions [87].

$I_i^+ \rightarrow I_f^+$	$\langle I_i \Vert E2 \Vert I_f \rangle$ (e fm^2)			$B(E2\downarrow; I_i^+ \rightarrow I_f^+)$ (W.u.)[a]				
	Present	SM	BMF	Present	Previous	SM	BMF	OCM [87]
$6_1^+ \rightarrow 4_1^+$	9.3	8.2	14.3	0.72	0.72 ± 0.02 [74] 0.74 ± 0.25 [80] 0.74 ± 0.03 [59] 0.77 ± 0.02 [73]	0.6	1.8	1.95
$6_2^+ \rightarrow 4_2^+$	75	63	92	50	50^{+35}_{-16} [71]	35	75	35.2
$2_3^+ \rightarrow 0_1^+$	4.2	4.1	1	0.4	0.4 ± 0.12 [80]	0.4	0.02	0.05
$2_3^+ \rightarrow 2_1^+$	18	11	5	7.5	7.5 ± 2.3 [80]	2.8	0.6	0.10
$2_3^+ \rightarrow 0_2^+$	12	7	9	2.0	2.0 ± 0.6 [80]	1.1	1.9	3.15
$2_3^+ \rightarrow 2_2^+$	20	24	31	9	9 ± 9[b] $\sim$2.3 [80]	13	22	
	$\langle I_i \Vert M1 \Vert I_f \rangle$ (μ_N)			$B(M1\downarrow; I_i^+ \rightarrow I_f^+)$ (W.u.)[c]				
$I_i^+ \rightarrow I_f^+$	Present	SM	BMF	Present	Previous	SM	BMF	
$2_2^+ \rightarrow 2_1^+$	0.97	0.78	-0.48	0.11	0.11 ± 0.01 [66]	0.07	0.03	
$2_3^+ \rightarrow 2_1^+$	0.16	0.21	-0.04	0.0029	0.0029^{+12}_{-7} [79]	0.005	0.0002	

[a]For ^{42}Ca, 1 W.u. $= 8.67\ e^2$ fm^4.
[b]Calculated from the branching ratio reported in Ref. [47] and the lifetime of the 2_3^+ state from Ref. [80].
[c]For ^{42}Ca, 1 W.u. $= 1.79 \mu_N^2$.

uncertainties of transition probabilities resulting from previous measurements.

The analysis yielded in particular two important quantities, determined for the first time: the $\langle 2_2^+ \Vert E2 \Vert 0_2^+ \rangle$ matrix element and the spectroscopic quadrupole moment of the 2_2^+ state. Their values are consistent with a highly-deformed character of the sideband in ^{42}Ca. In particular, the measured spectroscopic quadrupole moment of the 2_2^+ state corresponds to $\beta = 0.48(16)$. Other matrix elements obtained in the present analysis are, in general, in agreement with the results of earlier measurements, and in several cases the precision has been considerably improved, notably for transitions deexciting the 4_2^+ state.

The obtained set of reduced matrix elements reproduces all lifetimes presented in Table III within 1σ uncertainty, with the exception of the 2_2^+ state. The value obtained in the present analysis indicates a longer lifetime for this state (0.3 ps), which is still in agreement with the literature value within 3σ limit.

Almost all branching ratios presented in Table IV were reproduced within 1σ uncertainty, with only $I(4_2^+ \rightarrow 2_2^+)/I(4_2^+ \rightarrow 2_1^+)$ reproduced within 2σ and $I(4_1^+ \rightarrow 2_2^+)/I(4_1^+ \rightarrow 2_1^+)$ within 3σ limits. The latter are not consistent with the measured excitation cross sections to populate the 4_1^+, 4_2^+, and 2_2^+ states, and, consequently, if the measured branching ratios are imposed, the intensities of transitions depopulating these states cannot be reproduced and the total χ^2 value increases.

The obtained spectroscopic quadrupole moment of the 2_1^+ state was found in the agreement with the literature value within 1σ range. The experiment was not sensitive to $E2/M1$ multipole mixing ratios, hence the previously measured values should be understood as strong constraints rather than data points to be fitted, and consequently they were reproduced very well in the analysis.

IV. DISCUSSION

The obtained experimental results are discussed in the context of microscopic calculations performed with both shell-model (SM) and beyond-mean-field model (BMF) approaches. Comparisons with other calculations for ^{42}Ca are also presented, as well as an attempt to discuss the measured $E2$ matrix elements using a phenomenological two-state mixing model and the quadrupole sum rule method.

A. Large-scale shell-model calculations

In order to investigate the origins of the unexpected quadrupole collectivity, which has been observed in the semimagic nucleus ^{42}Ca, shell-model calculations were performed using the SDPF.MIX interaction in the $sdpf$ model space for neutrons and protons, with a virtual ^{28}Si core [24]. This interaction has proven successful in describing properties of the superdeformed bands in ^{40}Ca and ^{36}Ar and allows for the reproduction of the observed ground-state magnetic moments of ^{49,51}Ca and quadrupole moments of ^{47,49,51}Ca [88]. In spite of freezing of the excitations from the $1d_{5/2}$ orbit, and taking into account only excitations up to $8p - 8h$, the diagonalization of the matrix of dimension $O(4 \times 10^9)$, performed using the ANTOINE shell-model code [89,90], was challenging. This level of truncation was verified to ensure convergence of the calculated spectroscopic properties in ^{42}Ca. The electric effective charges used in the calculation were

TABLE VII. Quadrupole properties of the 2_2^+ and 2_3^+ states in ^{42}Ca, obtained in the present shell-model calculation.

J_i^+	2_2^+	2_3^+
Q_s (e fm^2)	−23.2	18.5
$B(E2, J_i^+ \to 0_i^+)$ (e^2 fm^4)	201.3	17.9
$B(E2, 3^+ \to J_i^+)$ (e^2 fm^4)	26.1	371.6

1.5e for protons and 0.5e for neutrons, whereas the effective gyromagnetic factors were $(g_\pi^s, g_\pi^l) = (5.5857, 1.0)$ for protons and $(g_\nu^s, g_\nu^l) = (-3.8263, 0.0)$ for neutrons.

The energies of excited states calculated within the shell model are in excellent agreement with the data, as shown in Fig. 10. The $E2$ matrix elements in the yrast band are underestimated, and those in the sideband overestimated with respect to the present experimental results. That means that the mixing between the two bands is not fully reproduced, as discussed in detail in Sec. IV D. On the other hand, the experimental $M1$ transition strengths are quite well reproduced by the present calculation, as shown in Table VI.

The quadrupole properties of the lowest nonyrast 2^+ states (Table VII), calculated in the laboratory frame, reveal collective aspects:

(i) $Q_s(2_3^+, K = 2)$ is nearly equal to $Q_s(2_2^+, K = 0)$, and they have opposite signs,
(ii) $Q_s(3_1^+, K = 2)$ is close to zero (0.14 e fm^2) and the low-lying 3_1^+ state is connected by a strong transition to the 2_3^+ state.

Furthermore, the intrinsic quadrupole moments Q_0 derived from calculated in-band $E2$ matrix elements via [91]

$$\langle I_f, K \| E2 \| I_i, K \rangle = \sqrt{2I_i + 1}(I_i, K, 2, 0 | I_f, K) \sqrt{\frac{5}{16\pi}} e Q_0 \tag{1}$$

or from the spectroscopic quadrupole moments via

$$Q_0 = \frac{(J+1)(2J+3)}{3K^2 - J(J+1)} Q_s(J) \tag{2}$$

are similar for the two excited bands, as presented in Table VIII.

These observations are consistent with a deformed character of excited states in ^{42}Ca and suggest that the structure built on the 2_3^+ state is a $K = 2$ γ band, with the configuration dominated by almost equal contributions of $6p - 4h$ and $8p - 6h$ excitations (∼40% each). The difference between the Q_0 values obtained from the transitional and diagonal $E2$ matrix elements, presented in Table VIII, may be attributed to triaxiality.

TABLE VIII. Intrinsic quadrupole moments Q_0 of the $K = 0$ and $K = 2$ bands extracted from calculated spectroscopic quadrupole moments and $B(E2)$ transition strengths.

	Q_0 from Q_s (e fm^2)	Q_0 from $B(E2)$ (e fm^2)
2_2^+	81	100
4_2^+	92	102
6_2^+	91	98
2_3^+	65	102
3_1^+		102

TABLE IX. β deformation parameter and the γ angle calculated using the Davydov-Filipov model, CHFSM, and Kumar-Cline sum rules, compared to the experimental values obtained from the sum rules (Tables XI and XII).

	0_1^+		0_2^+	
Davydov	0.09	12°	0.34	23°
CHFSM	0.03	60°	0.40	20°
Sum rules	0.22	15°	0.46	18°
Expt.	0.26(2)[a]	28(3)°	0.43(4)	$13(^{+5}_{-6})$°

[a]Deformation of the ground state is dynamic, as explained in detail in Sec. IV D, hence β and γ parameters presented here for the 0_1^+ state can be understood as the mean values of the deformation.

The quadrupole properties of the excited states calculated in the laboratory frame can be related to the nuclear shape in order to investigate the nature of observed structures, in particular that of the γ band. In Table IX we present the β and γ deformation parameters for the $0_{1,2}^+$ states in ^{42}Ca derived from the $E2$ matrix elements obtained in the present shell-model calculation using the Davydov-Filipov geometric model [92], Kumar and Cline's sum-rule approach [50,93], and constrained Hartree-Fock in the shell-model basis (CHFSM) [94,95].

In the Davydov-Filipov model [92], the γ angle can be extracted from the ratio $B(E2, 2_\gamma^+ \to 2^+)/B(E2, 2_\gamma^+ \to 0^+)$, and the β deformation parameter from the Q_0 intrinsic quadrupole moment, following

$$Q_0 = \sqrt{\frac{16\pi}{5}} \frac{3}{4\pi} Z e R_0^2 \beta \tag{3}$$

with $R_0 = 1.2A^{1/3}$. The CHFSM is a simple standard Hartree-Fock procedure restricted to the shell-model m-scheme configuration basis and used as a simplified alternative to exact diagonalizations [94,95]. The Hartree-Fock equations are solved and constrained on the quadrupole degrees of freedom, to obtain the minimal energies as a function of β and γ deformation parameters.

Finally, the quadrupole deformation parameters can be extracted using the $E2$ sum rules, proposed by Kumar [93], as detailed in Sec. IV D. It is worth noting that by using the strength function in the calculation of the sum rule we can get all the intermediate states reached from the initial states by $E2$ transitions. The values listed in Table IX result from the summation over all calculated intermediate states, unlike those in Tables XI and XII, where the sum was limited to states that were accessible experimentally.

As shown in Table IX, the deformation parameters obtained using the three methods are consistent for the 0_2^+ state, and they are in a good agreement with the experimental value. However, for the ground state we obtain β parameters close to zero using the Davydov-Filippov model and CHFSM [see Fig. 12(a)], while the sum rules yield a much larger value, closer to what is observed experimentally. This is related to the fact that

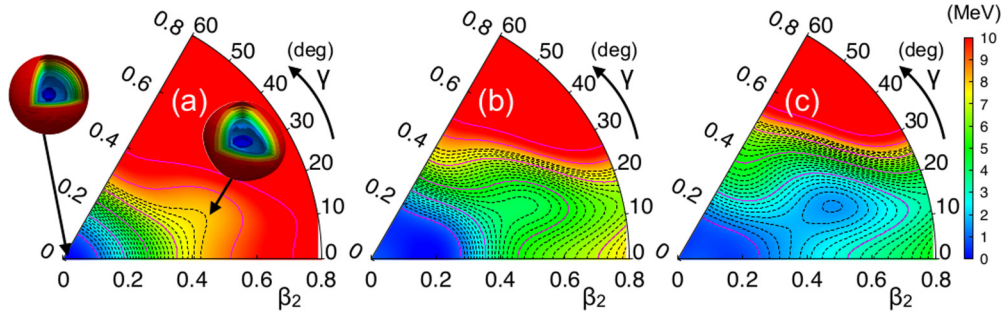

FIG. 8. Potential-energy surfaces computed with the Gogny D1S interaction and (a) particle number variation-after-projection (PN-VAP); (b) particle number and angular momentum projection (PNAMP) with $J = 0$; and (c) PNAMP with $J = 2$. Energies in each plot are normalized to that in its minimum and contour lines are separated by 0.25 MeV (dashed lines) and 2 MeV (solid lines), respectively. Inset in (a): Spatial densities corresponding to each minimum found in PN-VAP calculations.

the deformation of the 0_2^+ state has a static character, while the ground state exhibits large fluctuations about a spherical minimum, as discussed in Ref. [34].

B. Beyond-mean-field calculations

In the present work we have performed BMF calculations within the symmetry-conserving configuration mixing (SCCM) method [96] using the Gogny D1S interaction [97] to define the corresponding energy density functionals. This framework is very well suited to analyze the different states present in the low-lying spectra of atomic nuclei in terms of intrinsic shapes. In the SCCM method the nuclear states are obtained as linear combinations of particle number and angular momentum projected mean-field states. The coefficients of the linear combination are calculated self-consistently following the generator coordinate method (GCM) [98]. On the other hand, the mean-field states are found by solving the particle-number variation-after-projection (PN-VAP) Hartree-Fock-Bogolyubov (HFB) equations with constraints in the quadrupole operators parametrized by (β_2,γ) [99].

The PN-VAP energy defined in the (β_2,γ) plane yields qualitative information on the quadrupole properties of the nucleus under study. In Fig. 8(a) such a potential energy surface (PES) is plotted for the ^{42}Ca isotope. This PES shows a very well-defined spherical minimum, consistent with the semimagic character of this nucleus. In addition, a secondary minimum at $(\beta_2,\gamma) \approx (0.5,20^\circ)$ is found at a rather large excitation energy ($\sim$8 MeV). The specific shapes related to these minima (spherical and triaxially deformed) are better visualized if we represent the spatial densities that correspond to those HFB states [see inset in Fig. 8(a)].

If we project the intrinsic HFB states onto particle numbers and angular momentum, we obtain the PES represented in Figs. 8(b) and 8(c) for $J = 0$ and $J = 2$. Now the degeneracy around the spherical shape is larger within the triangle defined by $(\beta_2,\gamma) = (0,0^\circ)$, $(0.25,0^\circ)$, and $(0.2,60^\circ)$ and the correlation energy gained by the symmetry restoration brings the energy of the deformed state closer to that of the spherical one.

The last step in the SCCM calculation is the shape mixing within the GCM framework [96]. As a result, we obtain the spectrum shown in Fig. 10 and the electromagnetic matrix elements in the laboratory frame presented in Tables V–XIV. After this mixing the lowest excited states can be grouped into three bands built on top of the 0_1^+ ($\Delta J = 2$), 0_2^+ ($\Delta J = 2$), and 2_3^+ ($\Delta J = 1$) states, respectively. The ground-state band is characterized by small $E2$ transition probabilities and spectroscopic quadrupole moments, as expected for a spherical semimagic configuration. In contrast, larger in-band transitions are predicted in the second and third bands. In order to investigate the underlying shapes of the states belonging to these bands we analyze the collective wave functions (CWFs) of the band heads, as presented in Fig. 9. The

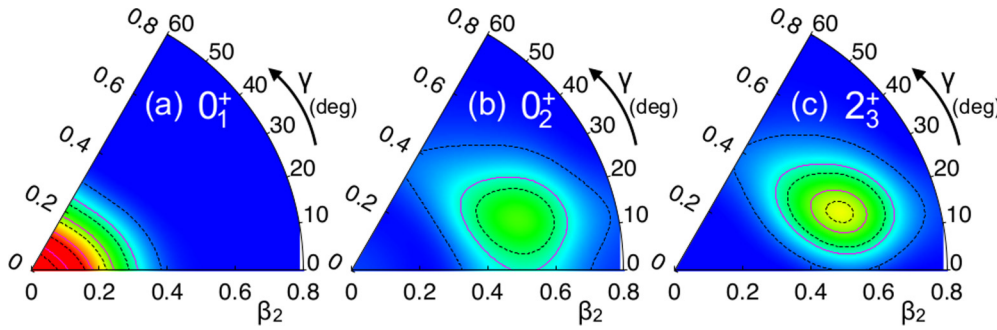

FIG. 9. Collective wave functions for the bandhead states obtained with BMF calculations with the Gogny D1S interaction. Red (blue) regions represent large (small) contributions to the wave functions.

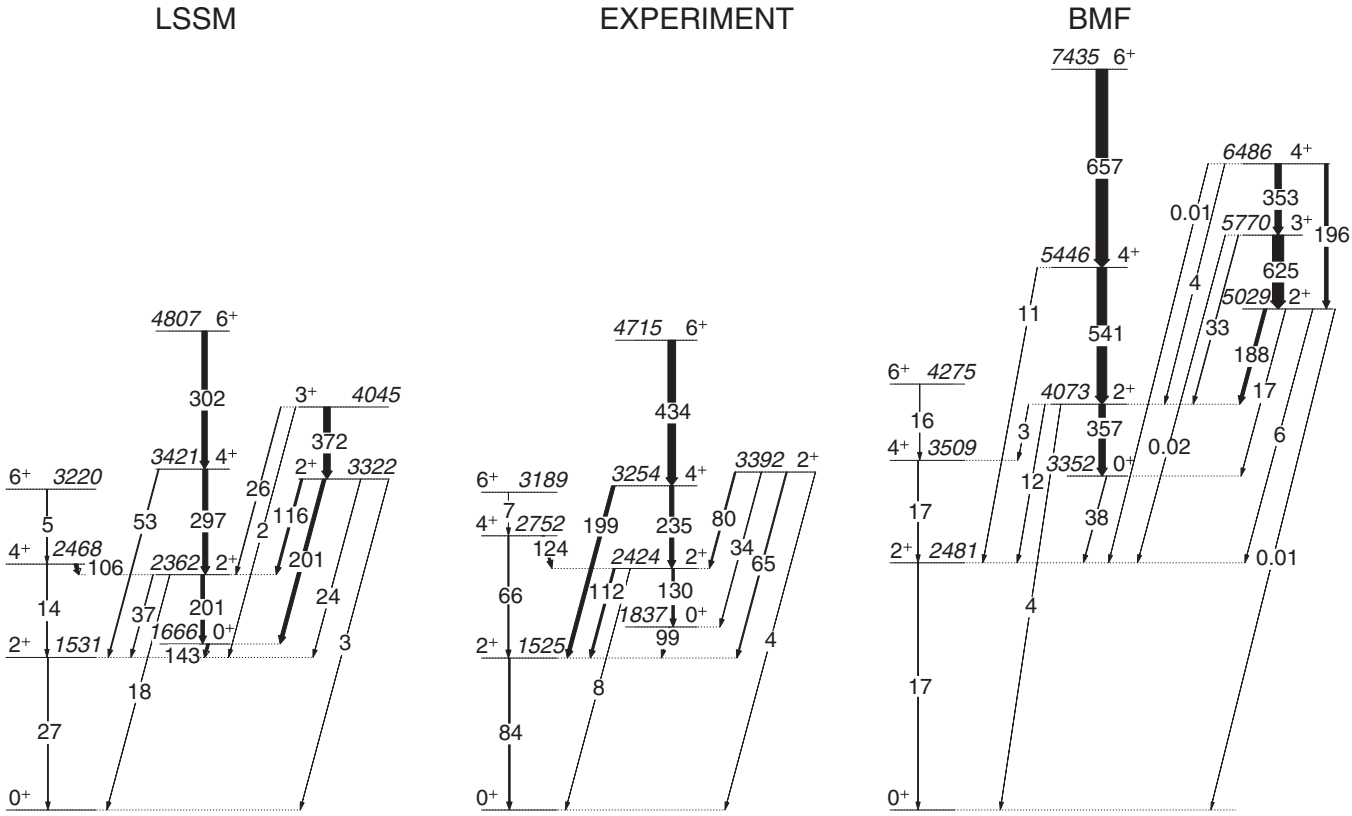

FIG. 10. Level schemes comparison: shell model (left), experiment (middle), beyond mean field (right). Level energies (in keV) are given in italics. The widths and labels of the arrows represent the measured and calculated $B(E2,\downarrow)$ values in e^2 fm^4.

CWFs represent the weights of each (β_2,γ) deformation in the nuclear states obtained within the SCCM framework. Hence, the most important contribution to the ground state comes from the spherical point and its surroundings [Fig. 9(a)]. For the states belonging to the second band $(0_2^+,2_2^+,\ldots)$ the most relevant shapes are found around $(\beta_2,\gamma)=(0.55,20^\circ)$, consistent with the strong electromagnetic transitions and negative spectroscopic quadrupole moments obtained in the present calculations. The third band shows CWFs rather similar to those in the second band, corroborating its character of a γ band $(K=2)$ built on the second band. The comparison of obtained transition probabilities and quadrupole moments with both the experimental results and SM calculations shows a very good qualitative agreement.

A comparison between the experimental level scheme and those obtained from theoretical calculations is presented in Fig. 10. The shell-model calculations reproduce the level scheme of ^{42}Ca remarkably well, while all level energies are overestimated by BMF calculations, with the ground-state band being too stretched and the sideband having a level spacing similar to what is observed experimentally, but appearing at a higher excitation energy. This can be explained by the lack of some degrees of freedom in the set of HFB wave functions used to perform the symmetry restoration and shape mixing. For example, the inclusion of cranking states allows for a better variational exploration of the states with $J\neq 0$ compressing the spectrum [100–102]. Moreover, energies of the excited 0^+ states can be affected by adding pairing fluctuations [103] and/or quasiparticle excitations explicitly [104]. Unfortunately, these improvements of the many-body method are very time consuming. We do not expect, however, that they would bring a change in the interpretation of the collective structure of ^{42}Ca.

C. Two-state mixing model

The $\langle Q^2\rangle$ quadrupole invariants experimentally determined for the $0_{1,2}^+$ and $2_{1,2}^+$ states in ^{42}Ca (Ref. [34]; see also Sec. IV D of the present paper) remain constant within the sideband, while for the ground-state band an important increase is observed between the 0_1^+ and the 2_1^+ states. This effect can be attributed to a possible mixing of the 2^+ states, consistent with one-neutron transfer reaction spectroscopy [67,105], therefore we attempt to interpret the measured $E2$ matrix elements in the framework of a phenomenological two-state mixing model (see Ref. [106] and the references therein).

The model is based on the assumption that the observed physical states can be expressed as linear combinations of two pure structures. The mixing of states with the same spin-parity I^π is described by a mixing angle θ_I, which can be calculated using the set of experimental matrix elements. To calculate mixing angles between the lowest 0^+ and 2^+ states in ^{42}Ca, the equations listed in Sec. V A of Ref. [106] were used, and the results are presented in Table X. The calculated mixing angle for the 0^+ states, $\cos^2(\theta_0)=0.88(4)$, indicates that 0^+ states in ^{42}Ca are weakly mixed, and is consistent with the

values obtained using theoretical matrix elements. The same quantity can be determined using the experimental value of the $\rho^2(E0;0_2^+ \to 0_1^+)$ transition strength, provided that the deformation parameters are known. In a two-level mixing scenario the $E0$ strength is given by [107,108]:

$$\rho^2(E0) = \left(\frac{3Z}{4\pi}\right)^2 \cos^2(\theta_0)\sin^2(\theta_0) \times \left[\left(\beta_1^2 - \beta_2^2\right) + \frac{5\sqrt{5}}{21\sqrt{\pi}}\left(\beta_1^3\cos\gamma_1 - \beta_2^3\cos\gamma_2\right)\right]^2, \tag{4}$$

where $\sin(\theta_0)$ is the amplitude of the admixed wave function with shape parameters (β_1,γ_1) (in this case, the 0_2^+ state) in the lower-lying level (the ground state) with (β_2,γ_2). The shape parameters for the 0_2^+ state are taken to be $\beta_1 = 0.43(4)$, and $\gamma_1 \approx 13(5)^\circ$ [34], whereas for the ground state the assumption is made that $\beta_2 = 0$. In this case, Eq. (4) reduces to

$$\rho^2(E0) \approx \left(\frac{3Z}{4\pi}\right)^2 \cos^2(\theta_0)\sin^2(\theta_0) \times \left[\beta_1^2 + \frac{5\sqrt{5}}{21\sqrt{\pi}}\beta_1^3\cos\gamma_1\right]^2. \tag{5}$$

Solving for $\cos^2(\theta_0)$ and using the experimental value of $1000\rho^2(E0;0_2^+ \to 0_1^+)$ of 135(12) [108] yields 0.84(4), which is consistent with 0.88(4) obtained in the analysis of the $E2$ matrix elements.

The obtained $\cos^2(\theta_2) = 0.39(8)$ value shows, however, that the simple two-level mixing model cannot be applied to the first two 2^+ states in ^{42}Ca, as this value suggests that the ground state has a 61% admixture of the deformed configuration, and vice versa. We suggest that this is related to the strong coupling of the 2_3^+ state to both 2_1^+ and 2_2^+: in both theoretical calculations the $B(E2;2_3^+ \to 2_2^+)$ value is much larger than $B(E2;2_3^+ \to 2_1^+)$, while the experimental transition strengths are similar. This would suggest that the mixing may involve all three 2^+ states, and, therefore, that the present model is too simple.

The same model has been applied to our results in Ref. [109]. In addition to reaching similar conclusions on the mixing of the 0^+ and 2^+ states, the author obtained weak mixing [$\cos^2(\theta_4) = 0.94(17)$] of the 4^+ states in ^{42}Ca. The consequences of changing the sign of the $\langle 0_1^+\|E2\|2_2^+\rangle$ matrix element were also explored: it leads to lower purity of the 0^+ states [$\cos^2(\theta_0) = 0.75(3)$] and slightly weaker mixing of the 2^+ states [$\cos^2(\theta_2) = 0.43(3)$], again showing that the two-state model is not applicable in this case.

For comparison, we can apply the two-state mixing model to matrix elements obtained from theoretical calculations. The results, presented in Table X, show that the two structures predicted by both theories mix weakly independent of the spin.

TABLE X. Mixing amplitudes for the 0^+ and 2^+ states in ^{42}Ca obtained from measured and calculated $E2$ matrix elements.

	Experiment	SM	BMF
$\cos^2(\theta_0)$	0.88(4)	0.85	0.96
$\cos^2(\theta_2)$	0.39(8)	0.83	0.97

D. Quadrupole sum rules

The quadrupole sum rules method [50,93,110] can be applied to the obtained $E2$ matrix elements in order to extract information on the charge distribution of the nucleus in specific states. The results obtained for the low-lying states in ^{42}Ca were published in Ref. [34]; here we would like to present the method in more detail, and analyze the contributions of individual matrix elements to the resulting invariants.

The quadrupole sum rules method is based on the fact that the electric multipole transition operator $E(\lambda = 2,\mu)$ is a spherical tensor and it can be represented using two parameters: Q, the overall quadrupole deformation parameter equivalent to the elongation parameter β in Bohr's model, and δ, which is related to the triaxiality parameter γ.

The expectation values of the quadrupole rotational invariants $\langle Q^2\rangle$ and $\langle Q^3\cos(3\delta)\rangle$ which describe the deformation of individual states in both the intrinsic and laboratory frames are determined using the set of $E2$ matrix elements by an expansion over all possible intermediate states using Wigner's $6j$ symbols:

$$\begin{aligned}\frac{1}{\sqrt{5}}\langle Q^2\rangle &= \langle I_i\|[E2\times E2]_0\|I_i\rangle \\ &= \frac{1}{\sqrt{2I_i+1}}\sum_j \langle I_i\|E2\|I_j\rangle\langle I_j\|E2\|I_i\rangle \\ &\quad\times \begin{Bmatrix} 2 & 2 & 0 \\ I_i & I_i & I_j \end{Bmatrix}, \end{aligned} \tag{6}$$

$$\begin{aligned}\langle Q^3\cos(3\delta)\rangle &= \langle I_i\|\{[E2\times E2]_2\times E2\}_0\|I_i\rangle \\ &= \mp\frac{\sqrt{35}}{\sqrt{2}}\frac{1}{\sqrt{2I_i+1}} \\ &\quad\times \sum_{jk}\langle I_i\|E2\|I_j\rangle\langle I_j\|E2\|I_k\rangle\langle I_k\|E2\|I_i\rangle \\ &\quad\times \begin{Bmatrix} 2 & 2 & 2 \\ I_i & I_j & I_k \end{Bmatrix}, \end{aligned} \tag{7}$$

where a negative sign corresponds to the integral spin system, while a positive sign corresponds to the half-integral spin one.

The first of the presented invariants is a measure of overall quadrupole deformation and is proportional to the sum of squared $E2$ matrix elements $\langle i\|E2\|t\rangle\langle t\|E2\|i\rangle$ over all intermediate states $|t\rangle$ that can be reached from the state in question $|i\rangle$ in a single $E2$ transition. The higher-order invariant $\langle Q^3\cos(3\delta)\rangle$ that provides information on triaxial asymmetry is constructed of triple products of $E2$ matrix elements ($\langle i\|E2\|t\rangle\langle t\|E2\|u\rangle\langle u\|E2\|i\rangle$, where $|i\rangle$ is the initial state, and $|t\rangle$ and $|u\rangle$ are intermediate states) and thus relative signs of $E2$ matrix elements entering the sum must be known.

The $\langle Q^2\rangle$ values were obtained for the 0^+ and 2^+ states in both bands, as presented in Table XII and in Fig. 11. Since the present measurement yielded relative signs of $E2$ matrix elements coupling the 0^+ and 2^+ states, it was also possible to

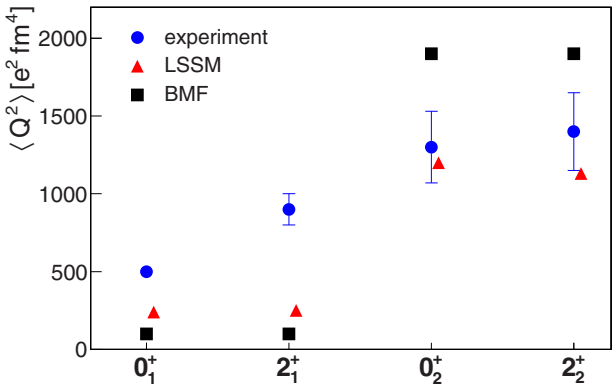

FIG. 11. Experimental and theoretical $\langle Q^2\rangle$ invariants for the $0^+_{1,2}$ and $2^+_{1,2}$ states in ^{42}Ca.

determine the $\langle Q^3\cos(3\delta)\rangle$ invariants for the 0^+_1 and 0^+_2 states (Tables XI and XII), as in Refs. [111,112].

In order to compare the deformation of each individual state with the theoretical results, the quadrupole sum rule method was applied to matrix elements resulting from theoretical calculations in the same way as it was done for the experimental ones. As described in Ref. [34], the nonzero $\langle Q^2\rangle$ value obtained for the 0^+_1 state corresponds to fluctuations about a spherical shape. This is consistent with the maximum triaxiality obtained for this state, which results from averaging over all possible deformed shapes. The confirmation of this interpretation comes from the fact that the magnitude of dispersion of $\langle Q^2\rangle$, defined as $\sigma(Q^2)=\sqrt{\langle Q^4\rangle-\langle Q^2\rangle^2}$ [113] is comparable to $\langle Q^2\rangle$, as presented in Table XII. The $\langle Q^4\rangle$ shape invariant is given by the fourth-order product:

$$\begin{aligned} P^4(J) =& \langle I_i\|\{(E2\times E2)^J\times(E2\times E2)^J\}^0\|I_i\rangle \\ =& \sum_{jkl}\frac{(2J+1)^{1/2}}{\sqrt{2I_i+1}}(-1)^{I_i-I_j} \\ & \times\langle I_i\|E2\|I_j\rangle\langle I_j\|E2\|I_k\rangle\langle I_k\|E2\|I_l\rangle\langle I_l\|E2\|I_i\rangle \\ & \times\begin{Bmatrix}2 & 2 & J\\ I_i & I_j & I_k\end{Bmatrix}\begin{Bmatrix}2 & 2 & J\\ I_i & I_j & I_l\end{Bmatrix} \end{aligned} \tag{8}$$

with $J=0,2,4$ being the spin that a pair of $E2$ operators is coupled to.

TABLE XI. Experimental and theoretical quadrupole invariants, $\langle Q^2\rangle$ (e^2 fm^4) and $\sigma(Q^2)$ (e^2 fm^4), for the $0^+_{1,2}$ and $2^+_{1,2}$ states in ^{42}Ca. Variances $\sigma(Q^2)$ are calculated from $\langle Q^4(0)\rangle$ listed in Table XII.

State	Expt.		SM		BMF	
	$\langle Q^2\rangle$	$\sigma(Q^2)$	$\langle Q^2\rangle$	$\sigma(Q^2)$	$\langle Q^2\rangle$	$\sigma(Q^2)$
0^+_1	480(20)	330(30)	240	470	100	250
2^+_1	890(100)		250	490	100	310
0^+_2	1310(250)	360(30)	1200	470	1910	520
2^+_2	1440(250)		1130	520	1970	310

TABLE XII. Experimental and theoretical $\langle Q^4\rangle$ invariants (10^4 e^4 fm^8) and $\langle\cos(3\delta)\rangle$ values, calculated from $\langle Q^3\cos(3\delta)\rangle$ as in Refs. [111,112].

		$\langle Q^4(0)\rangle$	$\langle Q^4(2)\rangle$	$\langle Q^4(4)\rangle$
0^+_1	expt.	35(6)		
	SM	30	30	20
	BMF	10	10	10
0^+_2	expt.	185(13)		
	SM	170	160	140
	BMF	390	380	380
	$\langle\cos(3\delta)\rangle_{\rm expt}$		$\langle\cos(3\delta)\rangle_{\rm SM}$	$\langle\cos(3\delta)\rangle_{\rm BMF}$
0^+_1	0.06(10)		0.34	0.34
0^+_2	0.79(13)		0.67	0.49

The three independent estimates of $\langle Q^4\rangle$ can be evaluated using $P^4(J)$ for $J=0,2,4$, via

$$\langle Q^4(0)\rangle = 5P^4(0), \tag{9}$$

$$\langle Q^4(2)\rangle = \frac{7\sqrt{5}}{2}P^4(2), \tag{10}$$

$$\langle Q^4(4)\rangle = \frac{35}{6}P^4(4). \tag{11}$$

The values of $\langle Q^4(4)\rangle$ obtained using the three possible intermediate spins J should be the same, which proves the consistency of the set of matrix elements and its completeness. The currently known set of experimentally obtained matrix elements, although rich, is only sufficient to obtain the expectation value of $\langle Q^4(0)\rangle$. The $\langle Q^4(0)\rangle$, $\langle Q^4(2)\rangle$ and $\langle Q^4(4)\rangle$ values obtained from sets of matrix elements resulting from BMF calculations are very similar for each of the two states, while the $\langle Q^4(4)\rangle$ obtained from large-scale shell model calculations is always lower than the other two: this is related to the fact that no matrix elements involving the 4^+_3 state were calculated within this approach.

The behavior of $\langle Q^2\rangle$ and its dispersion is remarkably consistent for both theoretical approaches, as shown in Fig. 11 and in Table XII. For the ground-state band, $\sigma(Q^2)_{SM}$ and $\sigma(Q^2)_{BMF}$ values are comparable with $\langle Q^2\rangle$, as one would expect for fluctuations about a spherical minimum of potential. For the sideband, however, the dispersion is much lower than the actual value, which is interpreted as a static deformation.

It should be noted that the deformation predicted by both theoretical approaches remains constant within each band. This is confirmed by the experimental results for the highly-deformed structure, but those for the ground-state band show that the $\langle Q^2\rangle$ for the 2^+_1 state is considerably larger than the value obtained for the ground state. This is consistent with the large mixing of the 2^+ states as discussed in Sec. IV C, suggesting that the 2^+_1 state has a considerable admixture of the well-deformed 2^+_2 and 2^+_3 states.

The contributions of individual matrix elements to the $\langle Q^2\rangle$ invariants for the $0^+_{1,2}$ and $2^+_{1,2}$ states in ^{42}Ca is presented in Table XIII, both for experimental and theoretical values.

TABLE XIII. Contribution of individual matrix elements to the values of the $\langle Q^2 \rangle$ shape invariants for 0_1^+, 2_1^+, 0_2^+, and 2_2^+ states in ^{42}Ca: experiment, SM, and BMF.

State	Component	Contribution to $\langle Q^2 \rangle$ (e^2 fm^4)		
	$E2 \times E2$	Experiment	SM	BMF
0_1^+	$\langle 0_1^+ \|\|E2\|\|2_1^+ \rangle \langle 2_1^+ \|\|E2\|\|0_1^+ \rangle$	418	134	80
	$\langle 0_1^+ \|\|E2\|\|2_2^+ \rangle \langle 2_2^+ \|\|E2\|\|0_1^+ \rangle$	35	89	19
	$\langle 0_1^+ \|\|E2\|\|2_3^+ \rangle \langle 2_3^+ \|\|E2\|\|0_1^+ \rangle$	27	17	1
	$\langle Q^2 \rangle =$	480(20)	240	100
2_1^+	$\langle 2_1^+ \|\|E2\|\|0_1^+ \rangle \langle 0_1^+ \|\|E2\|\|2_1^+ \rangle$	82	28	18
	$\langle 2_1^+ \|\|E2\|\|0_2^+ \rangle \langle 0_2^+ \|\|E2\|\|2_1^+ \rangle$	100	30	8
	$\langle 2_1^+ \|\|E2\|\|2_2^+ \rangle \langle 2_2^+ \|\|E2\|\|2_1^+ \rangle$	110	38	13
	$\langle 2_1^+ \|\|E2\|\|4_1^+ \rangle \langle 4_1^+ \|\|E2\|\|2_1^+ \rangle$	120	27	32
	$\langle 2_1^+ \|\|E2\|\|4_2^+ \rangle \langle 4_2^+ \|\|E2\|\|2_1^+ \rangle$	360	99	22
	$\langle 2_1^+ \|\|E2\|\|2_3^+ \rangle \langle 2_3^+ \|\|E2\|\|2_1^+ \rangle$	64	25	6
	$\langle 2_1^+ \|\|E2\|\|2_1^+ \rangle \langle 2_1^+ \|\|E2\|\|2_1^+ \rangle$	54	4	0
	$\langle 2_1^+ \|\|E2\|\|4_3^+ \rangle \langle 4_3^+ \|\|E2\|\|2_1^+ \rangle$			0.4
	$\langle 2_1^+ \|\|E2\|\|3_1^+ \rangle \langle 3_1^+ \|\|E2\|\|2_1^+ \rangle$			0.6
	$\langle Q^2 \rangle =$	890(100)	250	100
0_2^+	$\langle 0_2^+ \|\|E2\|\|2_1^+ \rangle \langle 2_1^+ \|\|E2\|\|0_2^+ \rangle$	488	142	40
	$\langle 0_2^+ \|\|E2\|\|2_2^+ \rangle \langle 2_2^+ \|\|E2\|\|0_2^+ \rangle$	655	1005	1780
	$\langle 0_2^+ \|\|E2\|\|2_3^+ \rangle \langle 2_3^+ \|\|E2\|\|0_2^+ \rangle$	168	52	89
	$\langle Q^2 \rangle =$	1310(230)	1200	1910
2_2^+	$\langle 2_2^+ \|\|E2\|\|0_1^+ \rangle \langle 0_1^+ \|\|E2\|\|2_2^+ \rangle$	8	18	4
	$\langle 2_2^+ \|\|E2\|\|2_1^+ \rangle \langle 2_1^+ \|\|E2\|\|2_2^+ \rangle$	119	38	12
	$\langle 2_2^+ \|\|E2\|\|4_1^+ \rangle \langle 4_1^+ \|\|E2\|\|2_2^+ \rangle$	67	3	3
	$\langle 2_2^+ \|\|E2\|\|0_2^+ \rangle \langle 0_2^+ \|\|E2\|\|2_2^+ \rangle$	136	207	370
	$\langle 2_2^+ \|\|E2\|\|4_2^+ \rangle \langle 4_2^+ \|\|E2\|\|2_2^+ \rangle$	421	551	990
	$\langle 2_2^+ \|\|E2\|\|2_3^+ \rangle \langle 2_3^+ \|\|E2\|\|2_2^+ \rangle$	97	119	190
	$\langle 2_2^+ \|\|E2\|\|2_2^+ \rangle \langle 2_2^+ \|\|E2\|\|2_2^+ \rangle$	592	193	351
	$\langle 2_1^+ \|\|E2\|\|4_3^+ \rangle \langle 4_3^+ \|\|E2\|\|2_1^+ \rangle$			5
	$\langle 2_1^+ \|\|E2\|\|3_1^+ \rangle \langle 3_1^+ \|\|E2\|\|2_1^+ \rangle$			45
	$\langle Q^2 \rangle =$	1440(250)	1130	1970

In almost all cases, the same matrix elements bring the most important contribution to the invariants calculated using experimental and theoretical matrix elements. The $\langle Q^2 \rangle$ for the ground state is dominated, as always, by the coupling to the 2_1^+ state, although its contribution to the experimental value is much larger than for those resulting from the calculations, especially using the SM (90% vs 55%). Different behavior is observed for the 0_2^+ state, where again the dominant contribution comes from the in-band matrix element, but the influence of matrix elements involving other 2^+ states is much larger for the experimental value, where they amount to 50% of the total, than for the theoretical calculations (16% and 6% for SM and BMF, respectively). This effect can be attributed to the mixing of 2^+ states being much larger in the experiment than in the theory. It should also be noted that the transition to the 2_3^+ state, although not observed in the present experiment, contributes to over 10% of the total $\langle Q^2 \rangle$ value for the 0_2^+ state.

For the 2_1^+ state, the dominant contribution to the invariant comes from an intraband transitional matrix element $\langle 2_1^+ \|E2\|4_2^+ \rangle$, amounting to about 40% of the total for both experimental and SM values. For the 2_2^+ state, the value of the spectroscopic quadrupole moment of this state has the largest influence on the experimental value, while it is the $\langle 4_2^+ \|E2\|2_2^+ \rangle$ in-band matrix element that contributes almost 50% of the total for both theoretical calculations; this difference is due to the more triaxial shape of the superdeformed band in the calculations than in the experiment, related to the reduction of the static quadrupole moments in this structure.

Additionally, we have evaluated the possible contribution of higher-lying states in the γ band to the $\langle Q^2 \rangle$ invariants using the matrix elements obtained from the BMF calculation. As shown in Table XIII, the contributions of the loops involving the 3_1^+ and 4_3^+ states bring less than 3% to the total $\langle Q^2 \rangle$ values, and therefore we expect the systematic error related to noncompleteness of the sum over intermediate states to be lower than the statistical error on the invariant.

For the $\langle Q^3 \cos(3\delta) \rangle$ invariant (see Table XIV), again there is a similarity between the calculations using experimental and theoretical matrix elements, with the dominant contributions coming from the same $E2 \times E2 \times E2$ loops, especially for the 0_2^+ state. For the 0_1^+ state, all $E2 \times E2 \times E2$ loops have similar influence on the final value of the invariant, and their contributions partly cancel out due to opposite signs. This is especially true for the invariant deduced from experimentally measured matrix elements. Here, in particular, we would like to note that the approximate formula proposed by Andrejtscheff and Petkov [114] to derive the $\langle Q^3 \cos(3\delta) \rangle$ invariant using only the first two $E2 \times E2 \times E2$ loops works very well in the case of ^{42}Ca (600 e^3 fm^6 from the approximate calculation vs 800 e^3 fm^6 from the full sum rules formalism, which translates into γ angles of 29.1° and 28.9°, respectively). The most notable difference concerns the $E2 \times E2 \times E2$ loops involving the spectroscopic quadrupole moment of the 2_1^+ state, which is the main contribution to the $\langle Q^3 \cos(3\delta) \rangle$ for the 0_2^+ state obtained from the experimental results, and is much less important for those resulting from the theoretical calculations. This is due to the fact that this matrix element is strongly underestimated by theory. The only difference regarding the sign is observed for two $E2 \times E2 \times E2$ loops involving the $\langle 2_2^+ \|E2\|0_1^+ \rangle$ matrix element, being the only matrix element whose experimentally measured sign has not been reproduced by the theory (see Table V).

For the 0_2^+ state, the main contributions to the $\langle Q^3 \cos(3\delta) \rangle$ invariant come from the $E2 \times E2 \times E2$ loops involving the $\langle 2_2^+ \|E2\|0_2^+ \rangle$ matrix element, as expected for a bandhead of a highly deformed structure, which is consistent both with theoretical calculations and experimental results. It should be noted that the contribution of this single loop is close to the value of the entire $\langle Q^3 \cos(3\delta) \rangle$ invariant, with all other contributions cancelling out to some extent; this is especially true for the invariants calculated using experimental values of $E2$ matrix elements, and those resulting from LSSM calculations.

The $E2 \times E2 \times E2$ loops involving the $\langle 2_2^+ \|E2\|2_1^+ \rangle$ and $\langle 2_3^+ \|E2\|2_1^+ \rangle$ matrix elements are more important for the calculations using experimental values of matrix elements than for those obtained from the theory. This is related to the mixing of 2^+ states being underestimated by the theory.

The spectroscopic quadrupole moment of the 2_3^+ state has not been measured experimentally, hence in the present analysis it was assumed to be equal to zero. However, the

TABLE XIV. Contribution of individual matrix elements to the values of the $\langle 0_1^+|Q^3\cos(3\delta)|0_1^+\rangle$ and $\langle 0_2^+|Q^3\cos(3\delta)|0_2^+\rangle$ shape invariants in ^{42}Ca: experiment, SM, and BMF.

State	Component	Contribution to $\langle Q^3\cos(3\delta)\rangle$ (e^3 fm^6)		
	$E2\times E2\times E2$	Experiment	SM	BMF
0_1^+	$\langle 0_1^+\|\|E2\|\|2_1^+\rangle\langle 2_1^+\|\|E2\|\|2_1^+\rangle\langle 2_1^+\|\|E2\|\|0_1^+\rangle$	5800	500	0
	$\langle 0_1^+\|\|E2\|\|2_1^+\rangle\langle 2_1^+\|\|E2\|\|2_2^+\rangle\langle 2_2^+\|\|E2\|\|0_1^+\rangle$	−5200	2500	500
	$\langle 0_1^+\|\|E2\|\|2_1^+\rangle\langle 2_1^+\|\|E2\|\|2_3^+\rangle\langle 2_3^+\|\|E2\|\|0_1^+\rangle$	−2700	−900	−100
	$\langle 0_1^+\|\|E2\|\|2_2^+\rangle\langle 2_2^+\|\|E2\|\|2_2^+\rangle\langle 2_2^+\|\|E2\|\|0_1^+\rangle$	1900	2200	700
	$\langle 0_1^+\|\|E2\|\|2_2^+\rangle\langle 2_2^+\|\|E2\|\|2_3^+\rangle\langle 2_3^+\|\|E2\|\|0_1^+\rangle$	1000	−1600	−200
	$\langle 0_1^+\|\|E2\|\|2_3^+\rangle\langle 2_3^+\|\|E2\|\|2_3^+\rangle\langle 2_3^+\|\|E2\|\|0_1^+\rangle$	0	−300	0
	sum of all contributions			
	$\langle 0_1^+\|Q^3\cos(3\delta)\|0_1^+\rangle$	800	2400	900
	$\langle\cos(3\delta)\rangle$	0.06(10)	0.34	0.34
0_2^+	$\langle 0_2^+\|\|E2\|\|2_1^+\rangle\langle 2_1^+\|\|E2\|\|2_1^+\rangle\langle 2_1^+\|\|E2\|\|0_2^+\rangle$	6800	500	0
	$\langle 0_2^+\|\|E2\|\|2_1^+\rangle\langle 2_1^+\|\|E2\|\|2_2^+\rangle\langle 2_2^+\|\|E2\|\|0_2^+\rangle$	22400	8600	3400
	$\langle 0_2^+\|\|E2\|\|2_1^+\rangle\langle 2_1^+\|\|E2\|\|2_3^+\rangle\langle 2_3^+\|\|E2\|\|0_2^+\rangle$	−8700	−1600	−500
	$\langle 0_2^+\|\|E2\|\|2_2^+\rangle\langle 2_2^+\|\|E2\|\|2_2^+\rangle\langle 2_2^+\|\|E2\|\|0_2^+\rangle$	30100	25800	62500
	$\langle 0_2^+\|\|E2\|\|2_2^+\rangle\langle 2_2^+\|\|E2\|\|2_3^+\rangle\langle 2_3^+\|\|E2\|\|0_2^+\rangle$	−12100	−9200	−20200
	$\langle 0_2^+\|\|E2\|\|2_3^+\rangle\langle 2_3^+\|\|E2\|\|2_3^+\rangle\langle 2_3^+\|\|E2\|\|0_2^+\rangle$	0	−1100	−3000
	sum of all contributions			
	$\langle 0_2^+\|Q^3\cos(3\delta)\|0_2^+\rangle$	38500	23000	42200
	$\langle\cos(3\delta)\rangle$	0.79(13)	0.67	0.49

contribution to the $\langle Q^3\cos(3\delta)\rangle$ invariant involving the corresponding matrix element is strongly suppressed independent of the $\langle 2_3^+\|\|E2\|\|2_3^+\rangle$ value, since it enters the sums multiplied by the $\langle 2_3^+\|\|E2\|\|0_1^+\rangle$ matrix element squared (or the $\langle 2_3^+\|\|E2\|\|0_2^+\rangle$ squared for the 0_2^+ state), which are small. This is confirmed by the theoretical calculations, that predict it to be on the level of 5–10% of the strongest contribution to $\langle Q^3\cos(3\delta)\rangle$ for both the 0_1^+ and 0_2^+ states.

The relative signs of all matrix elements involving the 2_3^+ state were adopted from the theory, thus the signs of the corresponding $E2\times E2\times E2$ loops are the same for the invariants obtained using experimental and theoretical values of matrix elements. A different combination of signs would have a minor influence on the $\langle Q^3\cos(3\delta)\rangle$ invariant for the 0_1^+ state, which would still correspond to a shape close to maximally triaxial. For the 0_2^+ state, changing the signs of the $E2\times E2\times E2$ loops involving the 2_3^+ state would lead to an increase of the $\langle Q^3\cos(3\delta)\rangle$ value closer to what would be expected for an axially symmetric nucleus, or even to nonphysical solutions of $\cos(3\delta)>1$. Measurement of the signs of matrix elements involving the 2_3^+ state remains a challenge for future Coulomb excitation experiments.

The $\langle Q^2\rangle$ and $\langle Q^3\cos(3\delta)\rangle$ invariants can be further converted to the β and γ collective model deformation parameters, as explained in detail in Ref. [110]. The $\beta=0.43(4)$ and $\gamma=13(^{+5}_{-6})^\circ$ deformation parameters obtained in this way for 0_2^+ show that the sideband in ^{42}Ca has a slightly triaxial superdeformed shape, and they can be directly compared to model predictions. Good overall agreement is found: both potential energy surface maps presented in Fig. 12 show a spherical minimum for the ground-state band. In addition, a triaxial minimum that is located at $\beta_2=0.4$ and $\gamma\approx 20^\circ$ for CHFSM [panel (a)] corresponds to the minimum at $\beta_2=0.5$, $\gamma=15^\circ$ for the BMF model [panel (b)].

E. Other theoretical approaches

The structure of ^{42}Ca was also studied in the framework of the generator coordinate method (GCM) with deformed-basis antisymmetrized molecular dynamics (AMD) wave functions [115], the $\alpha+{}^{38}$Ar orthogonality condition model (OCM) [87], and covariant relativistic energy density functional theory (CDFT) [116].

In the AMD-GCM approach [115] the Gogny D1S force was used as the effective interaction and the basis wave functions of the GCM were obtained via the energy variation with two types of constraints: the quadrupole deformation parameter of the total system, β, and the distance between the α and ^{38}Ar clusters. As a result, a rotational band of a predominantly

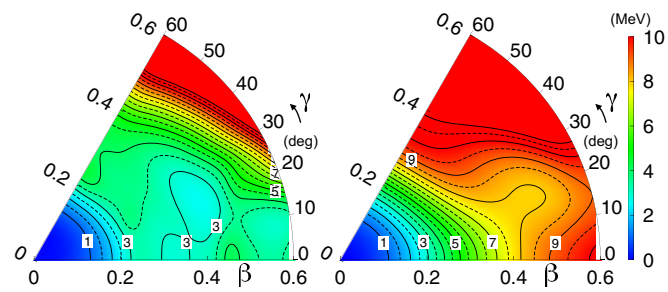

FIG. 12. Potential energy surfaces resulting from deformation-constrained Hartree-Fock calculations with (a) SM interaction, and (b) BMF, particle number projection method (PN-VAP), Gogny D1S interaction.

$6p-4h$ configuration and β deformation of about 0.4 was found with a bandhead at about 4 MeV excitation energy. By comparing the calculated intraband transition strengths with the experimental values, the authors identify this theoretical structure with the band built on the 0_2^+ state at 1837 keV. This is further supported by the fact that the 0_2^+ state is weakly populated in α transfer, consistent with the obtained low admixture of the α-^{38}Ar cluster structure component. The obtained value of $B(E2;4_2^+ \rightarrow 2_2^+) = 33.1$ W.u. is in good agreement with our present experimental findings [34], while that for $B(E2;2_2^+ \rightarrow 0_2^+) = 28.5$ W.u. is overestimated by almost a factor of 2. In addition, the calculations predicted a $K = 2$ sideband of the structure built on the 0_2^+ state, resulting from its triaxial deformation. On the other hand, the AMD calculations did not succeed in reproducing the level energies in ^{42}Ca, with the ground-state band built on $2p$ configuration being extremely compressed, and the sideband appearing at the energy twice as high as observed experimentally.

Another type of α-cluster model was applied to ^{42}Ca in Ref. [87]. The OCM theoretical calculations describe the cluster and shell-model states in a unified way. The ground-state band in ^{42}Ca is found to have a two-particle nature, while the sideband constructed on the 0_2^+ state has a predominantly $\alpha + ^{38}$Ar cluster structure. The 2_3^+ state is interpreted as resulting from coupling of an α cluster to the 2_1^+ state in ^{38}Ar. The calculated $B(E2)$ values are presented in Table V. The in-band transition strengths, both in the ground-state band and the sideband, are rather well reproduced, while the interband transitions are strongly overestimated. The calculated spectroscopic quadrupole moment of the 2_1^+ state is in good agreement with the experimental result, and its large negative value results mostly from the admixture of cluster components to the predominantly $2p$ 2_1^+ state. The $0_2^+ \rightarrow 0_1^+$ $E0$ transition strength was also reasonably well reproduced. The authors note that intraband transition rates are very sensitive to small admixtures of $2p$ and α-cluster wave functions to the dominant configuration, and the model should not be expected to give more than a qualitative prediction of these properties.

Highly-deformed structures in ^{42}Ca were also studied in the framework of the cranked relativistic mean-field theory (CRMF) [116]. The model does not assume the existence of cluster structures: their formation proceeds from microscopic single-nucleon degrees of freedom via many-body correlations. The sideband based on the 0_2^+ state in ^{42}Ca seems to correspond to the [4,3]a configuration in Ref. [116], predicted to appear at about 1 MeV excitation energy and to have a transitional quadrupole moment Q_t of about 1.5 e b [as compared to the experimental value of 1.13(10) e b]. Triaxial deformation of $\gamma \sim -20^\circ$ is expected for this structure, and the same is true for more deformed states in ^{42}Ca. Unfortunately, the predictions of this model do not include properties of the decay from the deformed structure to the yrast band.

V. SUMMARY

A Coulomb-excitation experiment to study electromagnetic properties of ^{42}Ca was performed at INFN Laboratori Nazionali di Legnaro. For the first time, the superdeformed and triaxial character of an excited structure in the $A \sim 40$ mass region was experimentally verified in a dedicated high-precision measurement. The phenomenological two band-mixing model gives further insight into the mixing of the wave functions, indicating a low degree of mixing between the 0^+ states and a significant one between the 2^+ states, but it is clearly too simple to describe all experimental data. A consistent description of the shape coexistence of a spherical ground state, exhibiting large fluctuations in the β-γ plane, and a rigid superdeformed sideband in ^{42}Ca could be achieved by performing sophisticated state-of-the-art theoretical calculations in the framework of the large scale shell-model and beyond-mean-field approach. Expectation values of the quadrupole invariants for the 0^+ and 2^+ states in the ground-state band and in the sideband in ^{42}Ca, related to the shape parameters, were derived in a model-independent way using the quadrupole sum rules formalism, and the application of this method to the theoretical results helps us to understand the complex structure of ^{42}Ca. The potential of Coulomb excitation as a tool to study superdeformation has been demonstrated for the first time.

ACKNOWLEDGMENTS

The authors would like to thank J. Dobaczewski and P. Garrett for the fruitful discussions. We also would like to thank the members of AGATA and EAGLE collaborations for their hard work for the project. Special gratitude goes to the INFN LNL and HIL Warsaw technical staff, for their support and help, in particular the accelerator crews for providing intense and good-quality ^{42}Ca and ^{32}S beams. K.H.-K. acknowledges support from the Research Council of Norway under Grant No. 213442. T.R.R. acknowledges computing time at GSI-Darmstadt and support from Spanish MINECO under Programa Ramon y Cajal 11420 and FIS-2014-53434-P (T.R.R.). We also acknowledge the support by Generalitat Valenciana, Spain, under Grant No. PROMETEOII/2014/019 and by the FEDER funds of the European Commission (A. Gadea), Spanish Ministerio de Economía y Competitividad under contract FPA2014-57196-C5 (A. Jungclaus, A Gadea), German Bundesministerium für Bildung und Forschung (BMBF) under Contract No. 05P12PKFNE TP4 (B. Birkenbach), the Polish National Science Centre under Projects No. 2011/03/B/ST2/01894, No. DEC-2013/10/M/ST2/00427, No. 2013/08/M/ST2/00591, No. UMO-2014/14/M/ST2/00738 (COPIN-INFN Collaboration), No. 2015/17/B/ST2/01534, No. 2016/22/M/ST200269, the UK STFC under Grants No. ST/J000124/1 and No. ST/L005735/1. The EAGLE Collaboration thanks the European Gamma-Ray Spectroscopy Pool (GAMMAPOOL) for the loan of Ge detectors.

[1] H. A. Jahn and E. Teller, Proc. R. Soc. London, Ser. A **161**, 220 (1937).

[2] S. M. Polikhanov *et al.*, Sov. Phys. JETP **15**, 1016 (1962).

[3] H. J. Specht, J. Weber, E. Konecny, and D. Heunemann, Phys. Lett. B **41**, 43 (1972).
[4] V. Metag, D. Habs, and H. J. Specht, Phys. Rep. **65**, 1 (1980).
[5] P. J. Twin, B. M. Nyako, A. H. Nelson, J. Simpson, M. A. Bentley, H. W. Cranmer-Gordon, P. D. Forsyth, D. Howe, A. R. Mokhtar, J. D. Morrison, J. F. Sharpey-Schafer, and G. Sletten, Phys. Rev. Lett. **57**, 811 (1986).
[6] P. J. Nolan, A. Kirwan, D. J. G. Love, A. H. Nelson, D. J. Unwin, and P. J. Twin, J. Phys. G **11**, L17 (1985).
[7] E. M. Beck, F. S. Stephens, J. C. Bacelar, M. A. Deleplanque, R. M. Diamond, J. E. Draper, C. Duyar, and R. J. McDonald, Phys. Rev. Lett. **58**, 2182 (1987).
[8] E. F. Moore, R. V. F. Janssens, R. R. Chasman, I. Ahmad, T. L. Khoo, F. L. H. Wolfs, D. Ye, K. B. Beard, U. Garg, M. W. Drigert, P. Benet, Z. W. Grabowski, and J. A. Cizewski, Phys. Rev. Lett. **63**, 360 (1989).
[9] T. L. Khoo *et al.*, Phys. Rev. Lett. **76**, 1583 (1996).
[10] A. Lopez-Martens *et al.*, Phys. Lett. B **380**, 18 (1996).
[11] R. B. Firestone, B. Singh, and S. Y. F. Chu, Nucl. Data Sheets **97**, 241 (2002).
[12] S. Raman, C. W. Nestor, and P. Tikkanen, At. Data Nucl. Data Tables **78**, 1 (2001).
[13] P. Fallon, Nucl. Phys. A **752**, 231c (2005).
[14] E. Ideguchi *et al.*, Phys. Rev. Lett. **87**, 222501 (2001).
[15] C. J. Chiara *et al.*, Phys. Rev. C **67**, 041303(R) (2003)
[16] C. E. Svensson *et al.*, Phys. Rev. Lett. **85**, 2693 (2000).
[17] C. E. Svensson *et al.*, Phys. Rev. C **63**, 061301(R) (2001).
[18] D. Rudolph *et al.*, Phys. Rev. C **65**, 034305 (2002).
[19] R. A. E. Austin, Ph.D. thesis, McMaster University, Hamilton, Ontario, Canada, 2004.
[20] E. Ideguchi *et al.*, Phys. Lett. B **686**, 18 (2010).
[21] C. D. O'Leary, M. A. Bentley, B. A. Brown, D. E. Appelbe, R. A. Bark, D. M. Cullen, S. Erturk, A. Maj, and A. C. Merchant, Phys. Rev. C **61**, 064314 (2000).
[22] A. Bisoi, M. S. Sarkar, S. Sarkar, S. Ray, M. R. Basu, D. Kanjilal, S. Nag, K. Selvakumar, A. Goswami, N. Madhavan, S. Muralithar, and R. K. Bhowmik, Phys. Rev. C **88**, 034303 (2013).
[23] E. Caurier, F. Nowacki, and A. Poves, Phys. Rev. Lett. **95**, 042502 (2005).
[24] E. Caurier, J. Menendez, F. Nowacki, and A. Poves, Phys. Rev. C **75**, 054317 (2007).
[25] T. Inakura, S. Mizutori, M. Yamagami, and K. Matsuyanagi, Nucl. Phys. A **710**, 261 (2002).
[26] R. R. Rodriguez-Guzman, J. L. Egido, and L. M. Robledo, Int. J. Mod. Phys. E **13**, 139 (2004).
[27] M. Bender, H. Flocard, and P. H. Heenen, Phys. Rev. C **68**, 044321 (2003).
[28] M. Kimura and H. Horiuchi, Nucl. Phys. **767**, 58 (2006).
[29] Y. Taniguchi, M. Kimura, Y. Kanada-En'yo, and H. Horiuchi, Phys. Rev. C **76**, 044317 (2007).
[30] M. Kimura and H. Horiuchi, Phys. Rev. C **69**, 051304 (2004).
[31] Y. Kanada-En'yo and M. Kimura, Phys. Rev. C **72**, 064322 (2005).
[32] Y. Taniguchi, Y. Kanada-En'yo, and M. Kimura, Prog. Theor. Phys. **121**, 533 (2009).
[33] Y. Taniguchi, Y. Kanada-En'yo, and M. Kimura, Phys. Rev. C **80**, 044316 (2009).
[34] K. Hadyńska-Klęk *et al.*, Phys. Rev. Lett. **117**, 062501 (2016).
[35] M. Lach *et al.*, Eur. Phys. J. A **16**, 309 (2003).
[36] M. Kmiecik *et al.*, Acta Phys. Pol. B **36**, 1169 (2005).
[37] K. Hadyńska-Klęk *et al.*, Acta Phys. Pol. B **42**, 817 (2011).
[38] K. Hadyńska-Klęk *et al.*, Acta Phys. Pol. B **44**, 617 (2013).
[39] D. Cline, Bull. Am. Phys. Soc. **14**, 726 (1969)
[40] S. Akkoyun *et al.*, Nucl. Instrum. Methods Phys. Res. A **668**, 26 (2012)
[41] A. Gadea *et al.*, Nucl. Instrum. Methods Phys. Res. A **654**, 88 (2011).
[42] J. J. Valiente-Dobón *et al.*, Acta Phys. Pol. B **37**, 225 (2006).
[43] I. J. Thompson, Comput. Phys. Rep. **7**, 167 (1988).
[44] R. A. Broglia and A. Winther, *Heavy Ion Reactions* (Benjamin/Cummings, Reading, MA, 1981), Vol. 1.
[45] G. Brown, A. Denning, and J. G. B. Haigh, Nucl. Phys. A **225**, 267 (1974).
[46] J. Mierzejewski *et al.*, Nucl. Instrum. Methods Phys. Res. A **659**, 84 (2011).
[47] W. J. Kossler, J. Winkler, and C. D. Kavaloski, Phys. Rev. **177**, 1725 (1969).
[48] Th. Kern, P. Betz, E. Bitterwolf, F. Glatz, and H. Röpke, Z. Phys. A **294**, 51 (1980).
[49] T. Czosnyka, D. Cline, and C. Y. Wu, Bull. Am. Phys. Soc. **28**, 745 (1982); www.slcj.uw.edu.pl/gosia
[50] D. Cline, Annu. Rev. Nucl. Part. Sci. **36**, 683 (1986).
[51] C. W. Towsley, D. Cline, and R. N. Horoshko, Nucl. Phys. A **204**, 574 (1973).
[52] K. Kawade, H. Yamamoto, K. Yoshikawa, K. Iizawa, I. Kitamura, S. Amemiya, T. Katoh, and Y. Yoshizawa, J. Phys. Soc. Jpn. **29**, 43 (1970).
[53] P. C. Simms, N. Benczer-Koller, and C. S. Wu, Phys. Rev. **121**, 1169 (1961).
[54] I. Asplund and T. Wiedling, Phys. Rev. **116**, 741 (1959).
[55] W. W. Daehnick and R. D. Rosa, Phys. Rev. C **31**, 1499 (1985).
[56] A. M. Sandorfi, C. J. Lister, D. E. Alburger, and E. K. Warburton, Phys. Rev. C **22**, 2213 (1980).
[57] P. C. Rogers and G. E. Gordon, Phys. Rev. **129**, 2653 (1963).
[58] J. W. Nelson, J. D. Oberholtzer, and H. S. Plendl, Nucl. Phys. A **62**, 434 (1965).
[59] R. A. Mendelson and R. T. Carpenter, Phys. Rev. **181**, 1552 (1969).
[60] E. K. Warburton, J. J. Kolata, and J. W. Olness, Phys. Rev. C **11**, 700 (1975).
[61] A. R. Poletti, B. A. Brown, D. B. Fossan, P. Gorodetzky, J. J. Kolata, J. W. Olness, and E. K. Warburton, Phys. Rev. C **10**, 997 (1974).
[62] P. Herges, H. V. Klapdor, and T. Oda, Nucl. Phys. A **372**, 253 (1981).
[63] H. H. Eggenhuisen, L. P. Ekström, G. A. P. Engelbertink, and H. J. M. Aarts, Nucl. Phys. A **305**, 245 (1978).
[64] R. L. Robinson, H. J. Kim, J. B. McGrory, G. J. Smith, W. T. Milner, R. O. Sayer, J. C. Wells, Jr., and J. Lin, Phys. Rev. C **13**, 1922 (1976).
[65] K. P. Lieb and M. Uhrmacher, Z. Phys. **267**, 399 (1974).
[66] H. L. Scott, R. N. Horoshko, and D. M. Van Patter, Nucl. Instr. Meth. **70**, 320 (1968).
[67] A. Jamshidi and W. P. Alford, Phys. Rev. C **8**, 1782 (1973).
[68] F. Pellegrini, F. Gentilin, and I. Filosofo, Phys. Rev. C **4**, 112 (1971).
[69] S. Cochavi, D. B. Fossan, S. H. Henson, D. E. Alburger, and E. K. Warburton, Phys. Rev. C **2**, 2241 (1970).

[70] J. D. McCullen and D. J. Donahue, Phys. Rev. C **8**, 1406 (1973).
[71] P. Betz, E. Bitterwolf, B. Busshardt, and H. Röpke, Z. Phys. A **276**, 295 (1976).
[72] R. Hartmann, K. P. Lieb, and H. Röpke, Nucl. Phys. **123**, 437 (1969).
[73] M. Marmor, S. Cochavi, and D. B. Fossan, Phys. Rev. Lett. **25**, 1033 (1970).
[74] T. Nomura, C. Gil, H. Saito, T. Yamazaki, and M. Ishihara, Phys. Rev. Lett. **25**, 1342 (1970).
[75] D. C. Williams, J. D. Knight, and W. T. Leland, Phys. Rev. **164**, 1419 (1967).
[76] F. R. Metzger and G. K. Tandon, Phys. Rev. **148**, 1133 (1966).
[77] P. M. Lewis, A. R. Poletti, M. J. Savage, and C. L. Woods, Nucl. Phys. A **443**, 210 (1985).
[78] P. M. Endt and C. van der Leun, Nucl. Phys. **214**, 1 (1973).
[79] N. Lawley, N. Dawson, G. D. Jones, I. G. Main, P. J. Mulhern, R. D. Symes, and M. F. Thomas, Nucl. Phys. **159**, 385 (1970).
[80] R. Hartmann and H. Grawe, Nucl. Phys. **164**, 209 (1971).
[81] A. Winther and J. de Boer, *Coulomb Excitation* (Academic, New York, 1966), p. 303.
[82] N. Benczer-Koller, M. Nessin, and T. H. Kruse, Phys. Rev. **123**, 262 (1961).
[83] H. D. Gräf, H. Feldmeier, P. Manakos, A. Richter, and E. Spamer, Nucl. Phys. A **295**, 319 (1978).
[84] M. Ulrickson, N. Benczer-Koller, J. R. MacDonald, and J. W. Tape, Phys. Rev. C **15**, 186 (1977).
[85] E. Clément *et al.*, Phys. Rev. C **94**, 054326 (2016).
[86] M. Zielińska, L. P. Gaffney, K. Wrzosek-Lipska, E. Clément, T. Grahn, N. Kesteloot, P. Napiorkowski, J. Pakarinen, P. Van Duppen, and N. Warr, Eur. Phys. J. A **52**, 99 (2016).
[87] T. Sakuda and S. Ohkubo, Phys. Rev. C **51**, 586 (1995).
[88] R. F. Garcia Ruiz *et al.*, Phys. Rev. C **91**, 041304(R) (2015).
[89] E. Caurier, G. Martinez-Pinedo, F. Nowacki, A. Poves, and A. P. Zuker, Rev. Mod. Phys. **77**, 427 (2005).
[90] E. Caurier and F. Nowacki, Acta Phys. Pol. B **30**, 705 (1999).
[91] A. Bohr and B. R. Mottelson, Kgl. Danske Videnskab. Selskab, Mat.-fys. Medd **27**, 16 (1953).
[92] A. S. Davydov and G. F. Filipov, Nucl. Phys. **8**, 237 (1958).
[93] K. Kumar, Phys. Rev. Lett. **28**, 249 (1972).
[94] G. Ripka, *Advances in Nuclear Physics*, (Plenum, New York, 1968), Vol. 1.
[95] B. Bounthong, Ph.D. thesis, Université de Strasbourg, 2016.
[96] T. R. Rodríguez and J. L. Egido, Phys. Rev. C **81**, 064323 (2010).
[97] J. F. Berger, M. Girod, and D. Gogny, Nucl. Phys. A **428**, 23 (1984).
[98] P. Ring and P. Schuck, *The Nuclear Many Body Problem* (Springer-Verlag, Berlin, 1980).
[99] M. Anguiano, J. L. Egido, and L. M. Robledo, Nucl. Phys. A **696**, 467 (2001).
[100] M. Borrajo, T. R. Rodríguez, and J. L. Egido, Phys. Lett. B **746**, 341 (2015).
[101] T. R. Rodríguez, Eur. Phys. J. A **52**, 190 (2016).
[102] J. L. Egido, M. Borrajo, and T. R. Rodríguez, Phys. Rev. Lett. **116**, 052502 (2016).
[103] N. L. Vaquero, T. R. Rodríguez, and J. L. Egido, Phys. Lett. B **704**, 520 (2011).
[104] F. Q. Chen and J. L. Egido, Phys. Rev. C **95**, 024307 (2017).
[105] C. Ellegaard, J. R. Lien, O. Nathan, G. Sletten, F. Ingebretsen, E. Osnes, P. O. Tjom, O. Hansen, and R. Stock, Phys. Lett. **40B**, 641 (1972).
[106] E. Clément *et al.*, Phys. Rev. C **75**, 054313 (2007).
[107] J. P. Davidson, Rev. Mod. Phys. **37**, 105 (1965).
[108] J. L. Wood, E. F. Zganjar, C. de Coster, and K. Heyde, Nucl. Phys. A **651**, 323 (1999).
[109] H. T. Fortune, Nucl. Phys. A **962**, 1 (2017).
[110] J. Srebrny and D. Cline, Int. J. Mod. Phys. **E20**, 422 (2011).
[111] N. Bree *et al.*, Phys. Rev. Lett. **112**, 162701 (2014).
[112] K. Wrzosek-Lipska *et al.*, Phys. Rev. C **86**, 064305 (2012).
[113] J. Srebrny *et al.*, Nucl. Phys. A **766**, 25 (2006).
[114] W. Andrejtscheff and P. Petkov, Phys. Rev. C **48**, 2531 (1993).
[115] Y. Taniguchi, Prog. Theor. Exp. Phys. **2014**, 073D01 (2014).
[116] D. Ray and A. V. Afanasjev, Phys. Rev. C **94**, 014310 (2016).